

Tesis
Que para obtener el grado de
Doctorado en Tecnología Avanzada

**Contribución a la caracterización
térmica de sólidos y detección de
grietas mediante termografía infrarroja
activa**

M. C. Kelly J. Martínez González

Directores: Dr. Ernesto Marín Moares y Dra. María Aranzazu
Mendioroz



Instituto Politécnico Nacional
Centro de Investigación en Ciencia Aplicada y Tecnología
Avanzada

Thesis
in fulfillment of the requirements for the degree of
Doctor in Advanced Technology

**Contribution to thermal
characterization of solids and cracks
detection using active infrared
thermography**

M. Sc. Kelly J. Martínez González

Advisors: Dr. Ernesto Marín and Dra. María Aranzazu
Mendioroz



Instituto Politécnico Nacional
Centro de Investigación en Ciencia Aplicada y Tecnología
Avanzada

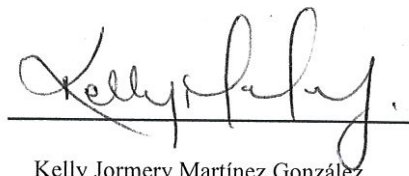


INSTITUTO POLITÉCNICO NACIONAL
SECRETARÍA DE INVESTIGACIÓN Y POSGRADO

CARTA CESIÓN DE DERECHOS

En la Ciudad de México el día 30 del mes noviembre del año 2018, el (la) que suscribe Kelly Jormery Martínez González alumna del Programa de Doctorado en Tecnología Avanzada con número de registro A150205, adscrito al Centro de Investigación en Ciencia Aplicada y Tecnología Avanzada Unidad Legaria CICATA-Legaria, manifiesta que es autor (a) intelectual del presente trabajo de Tesis bajo la dirección de Ernesto Marín Moares y María Aranzazu Mendioroz y cede los derechos del trabajo intitulado Contributions to thermal characterization of solids and cracks detection using active infrared thermography, al Instituto Politécnico Nacional para su difusión, con fines académicos y de investigación.

Los usuarios de la información no deben reproducir el contenido textual, gráficas o datos del trabajo sin el permiso expreso del autor y/o director del trabajo. Este puede ser obtenido escribiendo a la siguiente dirección kmartinez1709@gmail.com Si el permiso se otorga, el usuario deberá dar el agradecimiento correspondiente y citar la fuente del mismo.



Kelly Jormery Martínez González



INSTITUTO POLITÉCNICO NACIONAL SECRETARÍA DE INVESTIGACIÓN Y POSGRADO

ACTA DE REVISIÓN DE TESIS

En la Ciudad de México siendo las 18:00 horas del día 30 del mes de noviembre del 2018 se reunieron los miembros de la Comisión Revisora de la Tesis, designada por el Colegio de Profesores de Estudios de Posgrado e Investigación de CICATA-Legaria para examinar la tesis titulada:
Contribution to thermal characterization of solids and cracks detection using active infrared thermography

Presentada por el alumno:

Martínez González Kelly Jormery
Apellido paterno Apellido materno Nombre(s)

Con registro:

A	1	5	0	2	0	5
---	---	---	---	---	---	---

aspirante de:

SECRETARÍA Doctorado en Tecnología Avanzada GRADO

Después de intercambiar opiniones los miembros de la Comisión manifestaron **APROBAR LA TESIS**, en virtud de que satisface los requisitos señalados por las disposiciones reglamentarias vigentes.

LA COMISIÓN REVISORA

Directores de tesis

Dr. Ernesto Marín Moares

Dra. María Aranzazu Mendioroz Astigarraga

Dr. José Antonio Calderón Arenas

Dr. José Bruno Rojas Trigos

Salvador Alvarado R
Dr. Salvador Alvarado Ramírez

PRESIDENTE DEL COLEGIO DE PROFESORES

Dra. Mónica Rosalía Jaime Fonseca



SEP
CENTRO DE INVESTIGACIÓN EN CIENCIA
APLICADA Y TECNOLOGÍA AVANZADA
CICATA - LEGARIA

Contents

Abstract	2
Introduction	6
1 Theoretical framework	10
1.1 Some heat transfer concepts	10
1.1.1 Heat transfer mechanisms	10
1.1.2 The Biot's number	14
1.1.3 The heat diffusion equation	14
1.1.4 Thermal wave	15
1.1.5 The slope method for thermal diffusivity measurement.	18
1.1.6 Pulsed excitation.	19
1.2 Infrared thermography	21
1.2.1 General description	21
1.2.2 Lock-In Thermography	23
1.2.3 Vibrothermography	26
2 Influence of convection-radiation heat losses: A thermographic study.	29
2.1 Introduction	29
2.2 Heat diffusion equation with heat losses: theoretical analysis	30
2.3 Experimental configuration	34
2.4 Experimental results	37
2.5 Conclusions	39
3 Characterizing of open vertical cracks with burst vibrothermography	40
3.1 Introduction	40
3.2 Direct and inverse problems	42
3.3 Inversion of synthetic data	45
3.3.1 Effect of burst duration	46
3.3.2 Effect of noise level	48
3.3.3 Non-homogeneous heat sources	48
3.4 Experiments and inversion of experimental data	52
3.5 Conclusions	59

4	Characterization of slanted buried planar heat sources	60
4.1	Introduction	60
4.2	Theory	60
4.3	Simulations	62
4.4	Experiments	65
4.5	Conclusions	68
	Conclusions	69
	Products	70
	Bibliography	73

Agradecimientos

A mi familia, que son el motor de éstas metas. A mis padres, Luz y Jorge, por el gran apoyo que siempre me han brindado, no tengo palabras para explicar lo orgullosa que me siento de ser su hija. A mi hermano Cesar por transmitirme tenacidad, ser mi confidente y mi mejor amigo, siempre me ha dado el consejo necesario para llevar a cabalidad mis propósitos. A mi hermana Aylin, por su apoyo incondicional y su gran ejemplo de berraquera.

A mis amigos del laboratorio, por su amistad y momentos gratos. En especial a Angel, Adrian, Enrique y Joan por su amistad, apoyo y consejos. Entre todos siempre logramos que el laboratorio tuviera una linda armonía.

A todos mis amigos. En especial quiero agradecer a Jeniffer que siempre estuvo ahí para darme apoyo incondicional, a Cindy que me ha demostrado que la amistad no tiene distancias, y a Lorena que siempre me ha brindado una amistad sincera.

A mi asesor y director de tesis, el Dr Ernesto Marín, por su ayuda, esfuerzo, paciencia y dedicación. Le agradezco su incondicional apoyo y amistad en estos 6 años.

A mi co-directora de tesis, Arantza Mendioroz, por su ayuda e importantes aportes en mi trabajo de investigación.

Al Dr. Agustín Salazar y Dr. Bruno Rojas por sus contribuciones en el trabajo de investigación.

Al Dr. Gabriel Peña por su amistad y confianza depositada.

A todo el personal de CICATA-Legaria, por su amabilidad, colaboración y atención durante todo este tiempo.

Éste trabajo fue parcialmente financiado a través de proyectos de SIP-IPN (20170545 y 20181764) y CONACyT (205640, 2015-02-1042 y 2016-01-2482).

A CONACyT por la beca nacional y mixta, a COFAA-IPN COFAA-IPN por el apoyo económico mediante el programa BEIFI y en especial al IPN por permitirme ser parte de ésta gran familia.

Abstract

This thesis is concerned with some applications of the active infrared thermography technique for nondestructive measurement of thermal properties and buried cracks detection.

Some attempts have been reported to evaluate the influence of convective-radiative surface heat losses (CRHL) on the results of experiments performed with photothermal techniques, a group of methods widely used for physical and chemical characterization of materials. However, the effects of CRHL are often neglected. In a previous work (K. Martínez, Master Thesis, 2014) the influence of CRHL was studied using infrared (IR) thermometry and a mathematical model was developed to account for these losses, which also provides a simple criterion for neglecting them. The results of this model were in good agreement with those of measurements of the amplitude of the IR signal. However, the used experimental system consisted on a simple arrangement using an IR thermometer, with which it was not possible to determine the signal phase accurately. Here, we propose an experimental set-up that overcomes this limitation using a thermographic camera with incorporated lock-in possibilities and allows to determine the thermal diffusivity of materials, which also allows measurements under vacuum conditions in order to influence the heat convection contribution to CRHL. Using this system, it has been corroborated that the effect of CRHL is also evident in the phase of the IR signal at low frequencies.

On the other hand, it is well-known that the detection and characterization of cracks are highly valuable for industrial applications. In the last decade, the technique of vibrothermography has demonstrated its ability to detect defects that are elusive to other non-destructive evaluation (NDE) techniques. It can be used in a wide variety of materials, and especially, it is very suited and sensitive to the presence of kissing cracks as the relative vibration of their faces produces heat, which diffuses inside the material and can be detected as a temperature variation at its surface by means of an IR thermographic camera. In this work, open semicircular strip-shaped heat sources

were characterized, representing open half-penny cracks when the heat is produced at a certain contour, which is closer to a real situation with surface breaking cracks. Moreover, we determine not only the geometry, but also the absolute flux distribution and total power generated at vertical cracks. Continuing with this line will also make some computer simulations and experiments towards the detection of inclined cracks. It is possible to conclude that it is possible to find and characterize flat buried defects of different shapes and inclination using active IR thermography.

Resumen

Esta tesis trata sobre algunos usos de la termografía infrarroja (IR) activa para la medición de propiedades térmicas y la detección de grietas enterradas de manera no invasiva.

Se han reportado algunos intentos de evaluar la influencia de las pérdidas de calor por convección y radiación (CRHL, del inglés convective-radiative heat losses) sobre los resultados de experimentos realizados con técnicas fototérmicas, un grupo de métodos ampliamente utilizados para la caracterización física y química de materiales. Sin embargo, los efectos de las CRHL a menudo no son tenidos en cuenta. En un trabajo previo (K. Martínez, Tesis de Maestría, 2014) se estudió la influencia de las CRHL mediante la termometría infrarroja (IR) y se desarrolló un modelo matemático que tiene en cuenta estas pérdidas, y que también proporciona un criterio simple para su evaluación. Los resultados de este modelo se compararon favorablemente con los de las mediciones de la amplitud de la señal IR. Sin embargo, el sistema experimental utilizado consistió en un arreglo simple usando un termómetro IR, con el cual no era posible determinar exactamente la fase de la señal. En este trabajo proponemos una configuración experimental que supera esta limitación utilizando una cámara termográfica con posibilidades de detección sensible a fase y permite determinar la difusividad térmica de materiales, además permite mediciones bajo condiciones de vacío para influir en la contribución de la convección de calor a las CRHL. Utilizando este sistema, se ha corroborado que el efecto de las CRHL es también evidente en la fase de la señal IR a bajas frecuencias de modulación.

Por otra parte, es bien conocido que la detección y caracterización de grietas es altamente valioso en aplicaciones industriales. En la última década, la técnica de vibrotermografía ha sido de gran interés porque tiene la habilidad de encontrar defectos que son esquivos a otras técnicas de evaluación no destructiva (NDE, non-destructive evaluation), se puede utilizar en innumerables materiales, y en especial, es muy sensible a la presencia de grietas sub-superficiales ya que la vibración relativa de las caras produce

calor, la cual se difunde dentro del material y puede detectarse como una variación de temperatura en su superficie. Por tanto, en este trabajo, se caracterizaron fuentes de calor en forma de donas semicirculares, representando grietas abiertas de medio círculo donde el calor es producido en cierto contorno, lo cual es cercano a una situación real con grietas de ruptura de la superficie. Además, no solo se determinará la geometría, sino también la distribución del flujo absoluto y la potencia total generada en grietas verticales. También se harán algunas simulaciones y experimentos acerca de la detección de grietas inclinadas concluyendo que es posible caracterizar con termografía infrarroja activa defectos internos planos no solo de cualquier forma sino en cualquier inclinación.

Introduction

We could have a beginning of this technique, in 1800 when Dr Herschell, a british astronomer, discovered the infrared spectrum [1]. Using a mercury thermometer, he noted that the maximum elevation of temperature occurred beyond the red band here no radiation was visible. But only up to a century later, thanks to the discovery of the laws of Planck and Stefan-Boltzmann for the black-body radiation, the principle of thermography is presented: thermal radiation. These laws are very important for thermography since they allow to describe the formation of temperature images by measuring the radiative emission of a body. Modern IR imaging with electronic detectors started in the late 1940s. The first systems were for the military and consisted of line scanners with a single detector [2]. The enormous progress due to microsystem technologies toward the end of the twentieth century resulted in reliable quantitatively measuring infrared camera systems. Infrared thermal imaging has now become affordable to a wider public of specialized physicist, technicians and engineers for an ever-growing range of applications.

Infrared (IR) thermal imaging, also often called thermography for short, is defined as: “a nondestructive, nonintrusive, noncontact technique that allows the mapping of thermal patterns, i.e., thermograms, on the surface of objects, bodies or systems through the use of an infrared imaging instrument, such as an infrared camera” [3]. During the last years, the applications of IRT have been grown in different areas of knowledge and for the characterization of a broad spectrum of materials thanks to the constant technology improvement in different areas (computers, thermal sensors and cameras), the continuous price drop in instruments and because of the progressive acceptance of the technique by the industry. Thermography nowadays is applied in research and development as well as in a variety of different fields in industry, such as non-destructive testing [4], condition monitoring [5], and predictive maintenance [6], reducing energy costs of processes and buildings [7,8], detection of gaseous species [9],

and many more [10–12]. The theoretical and experimental fundamentals of IRT can be found elsewhere [13–16].

There are two main approaches for IRT: i- passive, in which materials and structures are naturally at different (higher or lower) temperature than the background, e.g. the human body is normally at a temperature higher than the ambient, hence it is easily detected by an IR camera without any additional stimulation and ii- active, in which an external stimulus is needed in order to produce a thermal contrast in the object surface, i.e. implies an artificial change of the object’s energetic equilibrium e.g. an object containing internal defects (such as voids, delaminations, foreign material inclusions, etc.) will require submission to a thermal disequilibrium in order to produce distinctive surface thermal patterns between the defects and the sound material that can be detected with an IR camera [3, 17]. Due to these reasons in this thesis we will use the second approach.

In this work, we focus on two very important applications:

The first is to use infrared thermography for the characterization of materials. Photothermal techniques are increasingly used in various fields to determine physical properties of materials [18, 19], hence there is a constant search to achieve improvements in existing techniques and to determine the thermal properties in a practical and efficient way [20, 21]. In most photothermal experiments, the spatial and temporal dependence of the temperature field is modelled by considering classical heat conduction, but consideration of sample’s surface convection and radiation heat losses (CRHL) to the sample’s surroundings is rather scarce [22]. Although some authors have studied the contributions of CRHLs [23–27]. Therefore, theoretical and experimental studies on the influence of CRHL on IRT experiments devoted to materials thermal characterization are still impetuous.

The second application is concerned to the characterization of buried cracks or defects, a theme of great interest for several industries for which many applications have been reported [28–30]. But most applications have been limited to find the existence of sub-superficial defects, without quantifying very important aspects of them such as their absolute flux distribution and total power generated, sizes, depth, inclination (if any) with respect of the surface, etc.

Due to this reason, in this work we will present some contributions in applications

with infrared thermography. The work is divided into four chapters: In chapter one, a brief summary of the key concepts is reviewed, which is important to understand the phenomenon of infrared thermography and the applications with which we will deal. The second chapter will be devoted to the study of the influence of CRHL on IRT experiments for thermal diffusivity measurements in solids. In the last two chapters the problem of the detection and quantification of buried cracks in solids will be studied.

Hypothesis

IR active thermography is useful and adequate for measuring thermal diffusivity, evaluate the influence of convective heat losses in photothermal experiments and allows the qualitative and quantitative characterization of buried defects.

Objectives

General objective

To apply the infrared active thermography technique to evaluate the effects of convective heat losses on the results of photothermal experiments and for the quantitative and qualitative characterization of buried defects in solids.

Particular objectives

- Design and implementation of an experimental set-up for active thermography measurements in front and rear detection configurations.
- Measurement of the rear signal amplitude and phase of different samples heated by periodically intensity modulated light.
- Comparison of the experimental results with those of a theoretical model that takes into account convective-radiative heat losses and determination of the samples thermal diffusivity.

- From the measurement of the temperature on the surface, quantitatively characterize the flow of heat generated in open semicircular strip-shaped cracks to the surface when excited by ultrasound
- Approach experimental situations with real cracks, we also consider inhomogeneous flux production analyzing different situations.
- Calculate the evolution of the surface temperature distribution produced by step-heated slanted buried planar heat sources and verification with experiments.

1 Theoretical framework

1.1 Some heat transfer concepts

1.1.1 Heat transfer mechanisms

Any temperature difference within a physical system is the cause of a transfer of energy in a form of heat from the region of higher temperature to the one of lower. This transport process takes place until thermodynamic equilibrium is reached, i.e. the system has become uniform temperature throughout. The heat flux density, Φ (units of W/m^2 , $\Phi = q/A$, where A is the surface area through which heat is transferred and q is the heat flux in W), is some function of the temperatures, T_1 and T_2 , of both the regions involved (we will suppose that $T_2 > T_1$). The mathematical form of the heat flux depends on the nature of the transport mechanism, which can be convection, radiation, conduction or a coupling of them [31].

Convection

Heat convection takes place by means of macroscopic fluid motion. It can be caused by an external source (forced convection) or by temperature dependent density variations in the fluid (free or natural convection). Convective heat flow, in its most simple form, i.e. heat transfer from surface of wetted area A and temperature T_2 , to a fluid with a temperature T_1 , for small temperature differences, $\Delta T = T_2 - T_1$, is given by the Newton's law of cooling [25],

$$\Phi_{\text{conv}} = \frac{q_{\text{conv}}}{A} = h_{\text{conv}} \Delta T \quad (1.1)$$

The convection heat transfer coefficient, h_{conv} , it is not a property of the fluid, but it is independent on ΔT . It's a parameter that is determined experimentally and

whose value depends on many variables such as the geometric surface of the surface, the nature of the movement of the fluid, the properties of the fluid and its maximum velocity.

Conduction

Heat can be transmitted through solids mainly by electrical carriers (electrons and holes) and elementary excitations such as spin waves and phonons (lattice waves). The energy transfer occurs from the more energetic to the less energetic particles in a substance due to interactions between them. Conduction takes place in solids, liquids and gases and is usually the most important form of thermal transport within a solid or solid objects in thermal contact [32]. Fourier's Law governs the stationary heat conduction through the opposite surfaces of a sample. It reads:

$$\Phi_{\text{cond}} = \frac{q_{\text{cond}}}{A} = -k\nabla T \quad (1.2)$$

The thermal conductivity, k [W/mK], is expressed as the quantity of heat transmitted per unit time, t , per unit area, A , and per unit temperature gradient, ∇T . It is important to note that Fourier's law is applicable to non-time varying temperature gradients. For one-dimensional steady state conduction in extended samples of homogeneous and isotropic materials and for small temperature gradients, Fourier's law can be integrated in each direction to its potential form. In rectangular coordinates it reads:

$$\Phi_{\text{cond}} = k \frac{T_2 - T_1}{x_2 - x_1} = \frac{k\Delta T}{L} = h_{\text{cond}}\Delta T \quad (1.3)$$

where T_1 and T_2 represent to planar isotherms at positions x_1 and x_2 , and

$$h_{\text{cond}} = k/L \quad (1.4)$$

is the conduction heat transfer coefficient.

For the heat flux by conduction one has:

$$q_{\text{cond}} = \frac{kA\Delta T}{L} = \frac{\Delta T}{R_{\text{cond}}} \quad (1.5)$$

where

$$R_{\text{cond}} = \frac{L}{Ak} = \frac{1}{Ah_{\text{cond}}} \quad (1.6)$$

is the thermal resistance of the sample. The Eq. 1.6 is often denoted as Ohm's law for thermal conduction following analogies existing with the law that relates electrical current with voltage through the electrical resistance. Note that this law holds only for stationary (DC) phenomena that can be straightforwardly described by Fourier's law (Eq. 1.2), which does not include any time derivative.

Radiation

Heat radiation is the continuous energy interchange by means of electromagnetic waves, so that this is the only heat transfer mechanism that does not require a material medium to take place. [31].

The spectral intensity emitted by a black body at a certain temperature T and wavelength λ , is given by Planck's law:

$$W_{\text{blackbody}}(\lambda, T) = \frac{2hc^2}{\lambda^5} \left(\frac{1}{e^{hc/\lambda k_B T} - 1} \right) \quad (1.7)$$

where c is speed of light, h the Planck constant, k_B Boltzmann constant. Here we see that the spectral intensity depends not only on the wavelength, but also on the absolute temperature of the black body. Fig. 1.1 shows the spectral intensity as a function of wavelength for different temperatures [33].

The spectral intensity is shifted towards shorter wavelengths as the temperature increases according to the Wien's displacement law stating that $T\lambda_{\text{max}} = b$, where b is the Wien's constant and λ_{max} is the wavelength corresponding to the maximum of the Planck's spectrum at the temperature T . The area under the curve of Fig. 1.1 is the net rate of heat flow density, Φ_{rad} , radiated by a black body. For a real body at the temperature T_0 surrounded by a medium at a temperature $T > T_0$, the density of heat flux by total radiation is given by the Stefan-Boltzmann Law:

$$\Phi_{\text{rad}} = \frac{q_{\text{rad}}}{A} = \epsilon\sigma (T_0^4 - T^4) \quad (1.8)$$

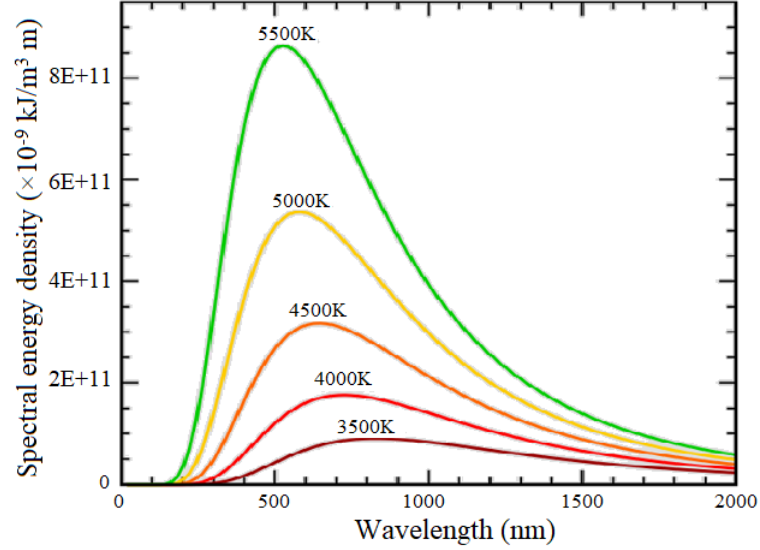


Figure 1.1: Spectral intensity of thermal radiation vs. wavelength

where, σ is the Stefan Boltzman constant, T is the surrounding temperature and, A is the surface area of the radiating object and is ϵ the total emissivity of its surface having absolute temperature T_0 . The emissivity, ϵ , being a parameter that characterizes the radiative properties of the surface of the material. For a black body $\epsilon = 1$ and the spectral intensity is given by the well-known Plank's law

A glance at Eq. 1.8 shows that if the temperature difference is small, so the 1.8 could be expanded in Taylor series around T_0 obtaining a linear relationship:

$$\Phi_{rad} = 4\sigma\epsilon T_0^3(T - T_0) = h_{rad}\Delta T \quad (1.9)$$

where,

$$h_{rad} = 4\sigma\epsilon T \quad (1.10)$$

has been introduced as a radiation heat transfer coefficient [21, 34].

Thus, the radiated energy in thermography experiments depends only on the sample surface temperature and on the emissivity. For this reason, the uncertainty about the emissivity of the sample surface would become a major problem, if absolute tempera-

tures were to be measured. However, only relative temperatures are evaluated in this work and, moreover, for small changes of temperature, just what we often need in lock-in thermography, the emissivity can be considered constant.

1.1.2 The Biot's number

We can write

$$H = h_{\text{conv}} + h_{\text{cond}} = \frac{1}{R_{\text{conv+rad}}} \quad (1.11)$$

where H and R are the heat transfer coefficient and the thermal resistance for convection-radiation heat transfer respectively.

Then, a so-called dimensionless Biot number can be defined as:

$$B_i = \frac{H}{h_{\text{cond}}} = R_T H \quad (1.12)$$

It represents the fraction of material thermal resistance that opposes to convection and radiation heat losses. If $B_i \ll 1$ then conduction is much more efficient than convection-radiation and in many cases the later mechanisms can be neglected.

1.1.3 The heat diffusion equation

Fourier's law only describes stationary heat conduction phenomena, so to describe the temperature depending on both, the spatial coordinate and the time, this Law must be combined with the Law of conservation of energy leading to the so-called heat diffusion equation. If we suppose that the changes of temperature are very small and thus to consider that the physical properties are constant, the heat diffusion equation in the absence of internal heat sources can be written as:

$$\frac{(\partial^2 T)}{(\partial x^2)} + \frac{(\partial^2 T)}{(\partial y^2)} + \frac{(\partial^2 T)}{(\partial z^2)} = \frac{1}{\alpha} \frac{\partial T}{\partial t} \quad (1.13)$$

where

$$\alpha = \frac{k}{C} \quad (1.14)$$

is the thermal diffusivity (m^2/s), which defined as a “rate” of propagation of heat through the body. This thermal parameter is related to the thermal conductivity, the specific heat c (J/gK) and the density ρ (g/m^3) through $\alpha = k/\rho c$. The heat capacity per volume unit is defined as: $C = \rho c$.

In particular, for the one-dimensional case in which the heat flow occurs only in the x -direction, equation 1.13 can be rewritten as:

$$\frac{\partial^2 T}{\partial x^2} - \frac{1}{\alpha} \frac{\partial T}{\partial t} = 0 \quad (1.15)$$

1.1.4 Thermal wave

The thermal “wave” is the solution of the heat diffusion equation with harmonic excitation, and has the characteristics of a highly damped wave [35].

Let us consider an isotropic homogeneous semi-infinite solid. The surface of said solid is being uniformly heated by an intensity modulated periodical light source given by:

$$\frac{I_o}{2} \text{Re}[1 + e^{i\omega t}] \quad (1.16)$$

where I_o (W/m^2) is the intensity of the light source and $\omega = 2\pi f$ is the angular frequency of modulation and t is the time. The hypothetical solid, of thermal diffusivity α , can absorb all incoming radiation on its surface and turn it into heat, in addition any heat transfer through radiation or convection can be neglected. Under these assumptions, the temperature distribution $T(x, t)$ (actually the temperature increase respecting the initial sample’s temperature) within the solid can be calculated using Eq. 1.15, i.e. the heat diffusion equation, using the following boundary condition:

$$-k \left. \frac{\partial \Delta T(x, t)}{\partial x} \right|_{x=0} = \frac{I_o}{2} \text{Re} [1 + e^{i\omega t}] \quad (1.17)$$

This condition express that the thermal energy generated at the surface of the solid diffuses into its bulk by diffusion and that heat losses by convection and radiation to the

surrounding medium are negligible. From now on, the operator $Re []$ will be omitted, taking into account the fact that the real part of the expressions of the temperature must be taken to obtain physical quantities. The solution of physical interest for applications in the field of photothermal techniques (e.g. the infrared active lock-in thermography technique dealing with in the next chapter) is the one related to the time dependent component. If we separate this component from the spatial distribution, the temperature can be expressed as:

$$T_{(x,t)} = \theta(x) e^{i\omega t} \quad (1.18)$$

Substituting Eq. 1.18 into Eq. 1.15 leads to

$$\frac{\partial^2 \theta_{(x,t)}}{(\partial x^2)} - q^2 \theta(x) = 0 \quad (1.19)$$

where the complex thermal wave number $q = \sqrt{i\omega/\alpha} = (1 + i)/\mu$. And

$$\mu = \sqrt{\frac{\alpha}{\pi f}} \quad (1.20)$$

is the thermal diffusion length. Using the boundary condition

$$-k \left. \frac{\partial \Delta T(x,t)}{\partial x} \right|_{x=0} = \frac{I_o}{2} \quad (1.21)$$

the Eq. 1.19 can be solved and substitution of the solution into Eq. 1.18 leads to

$$T_{(x,t)} = \frac{I_o}{2\varepsilon\sqrt{\omega}} e^{-\frac{x}{\mu}} e^{-i(\frac{x}{\mu} - \omega t + \frac{\pi}{4})} \quad (1.22)$$

where the parameter ε is the thermal effusivity of the sample. $\varepsilon = k/\sqrt{\alpha}$ ($\text{Ws}^{1/2}/\text{m}^2\text{K}$).

The Eq. 1.22 is the general solution for the oscillatory component of the heat diffusion equation. It has the form similar to that of a plane attenuated wave, and like other wave types, it has an oscillatory response in space e^{iqx} . This is what is known as thermal wave and the product of its first spatial derivative and thermal conductivity of the medium represent a heat flux wave.

Although they are not real waves themselves, they behave as waves and simplify the analysis of many systems. It can be said that they are temperature oscillations with wave-like features, without satisfying all the characteristics of a true wave, e.g. transporting energy [36]. In this work, the thermal wave approach will be used extensively for different experimental situations.

Suppose that we have an alternating heat flux, related to a periodic oscillating temperature field. In analogy to 1.5 defining thermal resistance for stationary heat conduction, one can define in the case of periodical heating the thermal impedance, Z_T as the temperature difference between two faces of a thermal conductor divided by the heat flux crossing the conductor. . Then the thermal impedance becomes the ratio between the change in thermal wave amplitude and the thermal wave flux. For the semi-infinite medium treated with above one gets [37],

$$Z_T = \frac{\Delta T(x = 0, t)}{-k \left. \frac{dT(x,t)}{dx} \right|_{x=0}} \quad (1.23)$$

Substituting Eq. 1.22 in Eq. 1.23 can be rewritten as:

$$Z_T = \frac{1 - i}{\varepsilon \sqrt{\omega}} = \frac{1}{\varepsilon \sqrt{\omega}} e^{-i\frac{\pi}{4}} \quad (1.24)$$

Note that, contrary to thermal resistance, which depends on thermal conductivity, in the thermal impedance definition the thermal effusivity becomes the relevant parameter.

The Eq. 1.22 can be rewritten as:

$$T(x, t) = \frac{I_o}{2} Z_T e^{-\frac{x}{\mu}} \cos\left(\frac{x}{\mu} + \omega t\right) \quad (1.25)$$

It shows that the thermal diffusion length, μ , being the distance at which the thermal wave amplitude decrease e -times (about 60%) from its value at the sample's surface (this is similar to the meaning of light absorption depth). The thermal wave wavelength is

$$\lambda = 2\pi\mu \quad (1.26)$$

Therefore, we can see that thermal waves are fully damped out in only one thermal wavelength.

1.1.5 The slope method for thermal diffusivity measurement.

Different variants of photothermal experimentation allow for the thermal characterization of materials. The following subsection provide a brief overview of some of the methods use. Not all the schemes discussed below are directly relevant to this work, however the phenomenological concepts introduced in each of them have been deemed noteworthy. In the next chapter we solve the heat diffusion equation considering the CRHL, this will allow characterizing materials with low conductivity at low frequencies.

The amplitude of the Eq. 1.22 can be expressed as:

$$A = \frac{I_o}{2\varepsilon\sqrt{2\pi f}} e^{-x\sqrt{\frac{\pi f}{\alpha}}} \quad (1.27)$$

and the phase-lag as:

$$\phi = -\frac{x}{\mu} - \frac{\pi}{4} \quad (1.28)$$

Suppose that for a periodical intensity modulated heat source at a given frequency, the amplitude (Eq. 1.27) and the phase (Eq. 1.28) of the photothermal signal are measured as a function of the distance x from the source. Note from Eqs. 1.27 and 1.28 that the graphs of $\ln(A)$ vs. x and ϕ vs. x become straight lines and that the thermal diffusivity can be straightforwardly calculated from their slopes $m = \sqrt{\frac{\pi f}{\alpha}}$ if f is well-known [38]. This is the basis of the well-known Angstrom or slope method for thermal diffusivity measurements. On the other hand, if x cannot be changed but its value at a distance L is well-known, and measurements are performed as a function of frequency, then the thermal diffusivity can be calculated from the slopes $m = -L\sqrt{\frac{\pi}{\alpha}}$ of the graphs $\ln(A\sqrt{f})$ vs. \sqrt{f} and ϕ vs. \sqrt{f} .

This procedure has been used by many researchers in photothermal techniques, and is closely related to the method developed by Angstrom [39] and Fourier [40] and recently proposed variants of them [25, 41].

1.1.6 Pulsed excitation.

Some techniques employ pulsed, rather than periodical heating. For these techniques, information about the sample under investigation is obtained by the analysis of the thermal transient following the pulse heating. A time-domain response $T(t)$ may be obtained from a frequency-domain response using a Fourier series expansion:

$$T(x, t) = \sum_n a(\omega_n) T(x, \omega_n, t) \quad (1.29)$$

in which the component $T(x, \omega_n, t)$ is a plane thermal wave of angular frequency ω_n propagating in the x-direction (Eq. 1.22) which is used as a basic function for the expansion:

$$T(x, \omega_n, t) = \frac{Q_0}{2k\sigma} e^{-\sigma x} e^{j\omega_n t} \quad (1.30)$$

and where $a(\omega_n)$ is a measure of the strength of this component in the transient concerned.

The spectrum of thermal wave modulation frequencies is continuous and the Fourier series expansion (Eq 1.29) can be replaced by an integral transform. The resulting integrals can often be easily evaluated in the complex plane by the Laplace inverse transform method. The Laplace transform of a function $f(t)$ and its inverse are defined by the following equations:

$$f(s) = L\{f(t)\} = \int_{c-j\infty}^{c+j\infty} e^{-st} f(t) dt \quad (1.31)$$

$$f(t) = L^{-1}\{f(s)\} = \frac{1}{2\pi j} \int_{c-j\infty}^{c+j\infty} e^{-st} f(s) ds \quad (1.32)$$

where $t > 0$ and the symbols L and L^{-1} are used to denote the Laplace transform and its inverse respectively. The integration in Eq. 1.32, Bromwich's integral formula, is along a line $c + jy$ in the complex plane, with c chosen to be to the right of all singularities but otherwise arbitrary. These transforms provide a simple route for obtaining the

transient solutions to problems that have already been solved in the frequency-domain. If we set $s = j\omega$ we can then write the following general expression for the Laplace transformed surface temperature $T(s)$:

$$T(s) = Q(s)Z(s) \quad (1.33)$$

where $Q(s)$ and $Z(s)$ are the Laplace transformed heat source and thermal transfer function for the sample respectively. The time-domain surface temperature is simply:

$$T(t) = L^{-1} \{Q(s)Z(s)\} \quad (1.34)$$

To illustrate the above approach we will consider the transient thermal response of a semi-infinite solid to a Dirac delta surface heating pulse. This is an important example as the excitations produced in many pulsed laser experiments are modelled well by a Dirac delta function. A Dirac delta thermal impulse on the surface plane of the solid, $x = 0$, at time $t = 0$ is equivalent to a continuous broad frequency spectrum of equal energy thermal wave components that are all in phase only when $t = 0$ at $x = 0$. The temperature at a depth x and at a time t after the pulse excitation can be obtained by a simple addition of the thermal wave amplitudes at (x, t) :

$$T(x, t) = \sum_{n=0}^{\infty} \frac{Q_0}{2k\sigma_n} e^{-\sigma_n x} e^{j\omega_n t} \quad (1.35)$$

with becomes:

$$T(x, t) = \frac{1}{\pi} \int_0^{\infty} \frac{Q_0}{2k\sigma(\omega)} e^{-\sigma(\omega)x} e^{j\omega t} d\omega \quad (1.36)$$

$$= \frac{1}{2\pi j} \int_0^{\infty} e^{st} \frac{Q_0}{2\sigma(s)} e^{-\sigma(s)x} ds \quad (1.37)$$

$$= Q_0 L^{-1} \left[\frac{e^{-\sigma x}}{2k\sigma} \right] \quad (1.38)$$

demonstrating the role of the inverse Laplace transform in obtaining a transient response

from a known frequency response. Setting $\sigma = \sqrt{s/\alpha}$ and evaluating the inverse transform leads to the solution corresponding to a Dirac delta pulse [22, 42]:

$$T(x, t) = \frac{Q_0}{2\sqrt{\pi\rho ckt}} e^{-\frac{x^2}{4\alpha t}} \quad (1.39)$$

$$\mu_t = 2\sqrt{\alpha t} \quad (1.40)$$

Then,

$$T(x, t) = \frac{Q_0}{2\sqrt{\pi\rho ckt}} e^{-\frac{x^2}{\mu_t^2}} \quad (1.41)$$

This characteristic distance is defined as the thermal diffusion length (for pulsed excitation) or characteristic heat propagation depth [43].

1.2 Infrared thermography

1.2.1 General description

Infrared (IR) thermography is a nondestructive testing (NDT) imaging technique that allows the visualization of heat patterns on an object or a scene by measuring the radiated heat flux. This can be done in two ways: passive and active. In the first one, there is not illumination or stimulation, e. g. the human body has a higher temperature than the ambient, and hence it radiates heat that is easily detected by an IR camera without any additional stimulation. In the second approach (active), the analyzed object is subjected to heating by an external agent. This heating can be performed using a single pulse or burst of heat or repeating it periodically. In the second case, thermal waves are generated within the sample that propagates through it by conduction and induce periodical oscillations in the heat flux radiated by the sample's surface that can be measured with an infrared camera with high frame rate and thermal resolution. For example, in this thesis ultrasonic waves will be generated by mechanical vibration (vibrothermography) to excite heat in internal features, e.g. cracks. To recover the amplitude and phase of the temperature field at the heating modulation frequency (for

example for thermal diffusivity measurement by the slope method) phase resolved measurements must be done, for example by lock-in synchronous detection. One advantage of active lock-in thermography is that detailed examinations can be performed with a relatively small energy input to the object. This allows the examination of thermally sensitive components and the use of relatively simple heat sources. On the other hand, for non-destructive testing purposes, the phase image is often more informative than the amplitude one, which strongly depends on the local IR emissivity.

As depicted in Figure 2, there are three classical active thermographic techniques based on these two excitation modes: lock-in thermography and pulsed thermography, which are optical techniques applied externally; and vibrothermography, which uses ultrasonic waves (amplitude modulated or pulses) to excite internal features. Lock-in thermography is presented first [44].

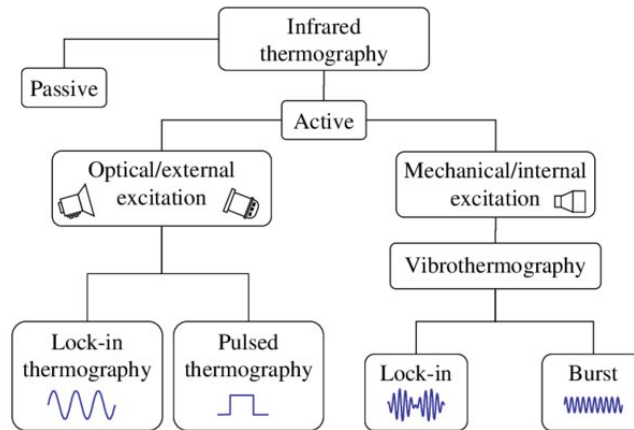


Figure 1.2: Infrared thermography approaches. [44]

Infrared radiation emitted from the sample surface must travel to the detector through the atmosphere. Fig. 1.3 shows a diagram of the atmospheric absorption bands. As can be observed, there are three main areas where low atmospheric absorption occurs, the so-called atmospheric windows (from 1 to 2.5 μm , from 3 to 5 μm and from 8 to 12 μm) and IR cameras are equipped with detector materials coincident with these atmospheric windows.

In this work two thermographic cameras have been used. Their main characteristics are given in Tab. 1.1. The cameras SC5000 and J550M are robust cameras that provide

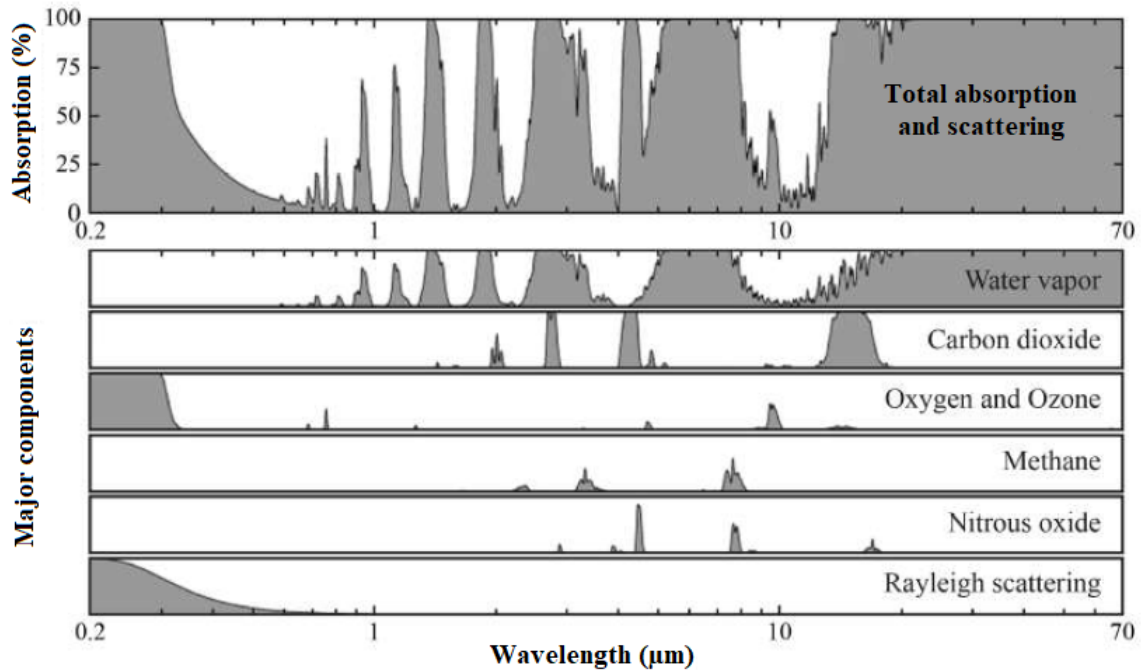


Figure 1.3: Absorption spectrum of the atmosphere and its major absorption components

low noise and high pixel speed without compromising sensitivity. They have high acquisition speed and accuracy, and allow to do thermal mapping of the sample, a great advantage over other photothermal techniques based in the detection of infrared radiation. Even small temperature differences can be visualized using the cooled Indium Antimonide (InSb) detectors. InSb is the most highly developed and widely used semiconductor material in the 1-5 μm spectral region and one of the most sensitive detector materials available in the medium-wave spectral region [2]. Compared to $\text{Hg}_{1-x}\text{Cd}_x\text{Te}$, the technology of InSb is less complicated [45] and enables large detector arrays of reasonable uniformity with more than 1 megapixel.

1.2.2 Lock-In Thermography

The Lock-In Amplification (LIA) technique allows the recovery of amplitude modulated signals on a known carrier frequency, f , in an environment where the signal to noise ratio (SNR) is very low. A simple schema to illustrate the LIA operating principle is

Camera	SC5000	JADE J550M
Sensor type	InSb	InSb
Wavelength	2.5-5.1 μ m	3.5-5 μ m
Pixel Resolution	320x256	320x256
Frame rate (max.)	Hasta 380 Hz	Hasta 400 Hz
NETD	< 20mK	< 25mK

Table 1.1: Description of the cameras used in this work.

shown in Fig. 1.4 [46].

Suppose that the carrier wave, $S_{\text{ref}}(t)$, is a sinusoid of frequency, f , and unit amplitude:

$$S_{\text{ref}}(t) = \sin(2\pi ft) \quad (1.42)$$

generated using the signal driving the periodical excitation element, e.g. a laser. The signal resulting from the experiment will be an amplitude modulated phase shifted signal and incoherent random noise, $G(t)$, whose frequency is, for the most part, different from that of the reference.

$$S_{\text{ref}}(t) = A \sin(2\pi ft + \phi) + G(t) \quad (1.43)$$

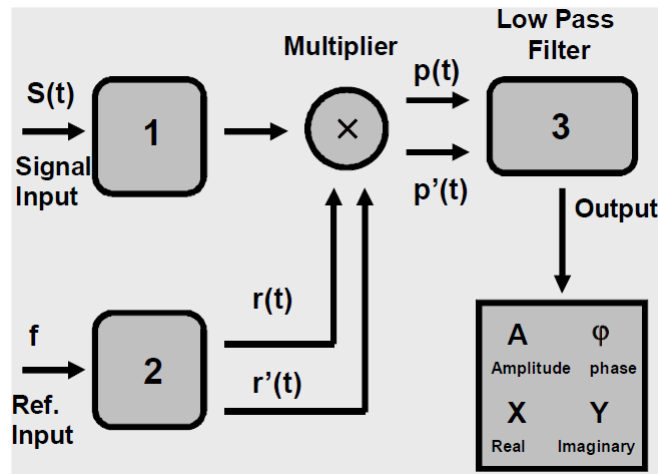


Figure 1.4: LIA block diagram

In a LIA, the input signal is first multiplied by the in-phase reference signal and by a signal in quadrature with this, i.e. shifted by 90° , $S_{\text{ref}'}(t)$, i.e:

$$\begin{aligned} P_1(t) &= S_{\text{in}}(t) \times S_{\text{ref}}(t) \\ P_Q(t) &= S_{\text{in}}(t) \times S_{\text{ref}'}(t) \end{aligned} \quad (1.44)$$

It can be demonstrated that for these products result:

$$\begin{aligned} P_1(t) &= \frac{1}{2} (A \cos(\phi) - A \cos(4\pi f + \phi)) f + S_{\text{ref}}(t)G(t) \\ P_Q(t) &= \frac{1}{2} (A \sin(\phi) - A \sin(4\pi f + \phi)) f + S_{\text{ref}'}(t)G(t) \end{aligned} \quad (1.45)$$

Note that in the previous equations all terms are oscillatory except for the first term in each of the equations, which are only generated when two components of equal frequency are multiplied. These oscillatory terms (also G including terms) can be eliminated by low-pass filtering the signals P and P' so that it is obtained:

$$P=I = \frac{A}{2} \cos(\phi) \quad (1.46)$$

$$P' = Q = \frac{A}{2} \sin(\phi) \quad (1.47)$$

Notice that any harmonic response from the experiment would effectively be handled as noise in LIA. These two relations can be considered a simple two equation system with two unknown variables. Solving for A and ϕ we have:

$$\begin{aligned} A &= \frac{1}{2} \sqrt{I^2 + Q^2} \\ \phi &= \tan^{-1} \left(\frac{Q}{I} \right) \end{aligned} \quad (1.48)$$

Depending on the modulation frequency, a LIA measurement can be a lengthy proce-

dure. To determine the offset values I and Q with good precision a sufficient number of cycles must be used.

In a IR thermographic camera each pixel element may act as a single thermal wave detector. However, one can not connect each detector element with its own lock-in amplifier required to correlate the local temperature response to the excitation input. To avoid this difficulty one has to perform a Fourier analysis on the time dependence of the temperature at each pixel in order to obtain magnitude and phase of temperature modulation. Such a procedure must be very fast if the Fourier analysis at large pixel's numbers should not take more time than the measurement itself. There are other features that lock-in thermography should consider. It must be able to reduce the average noise, A_{noise} well below the noise equivalent temperature difference ($NETD$) of the camera, depending on the number of images or frames, N , analyzed, being [47]:

$$A_{noise} = \frac{2}{\sqrt{N}} NETD \quad (1.49)$$

The NETD allows us to predict the average amplitude of the random noise level after a certain acquisition time at a given frame-rate. This is only valid for random white noise; other noise sources will not behave accordingly [47]. Another important point to be considered is that the camera's speed limits the modulation frequency. The Nyquist sampling theorem tells us that the sampling rate of a band-limited signal must be at least twice as high in order to digitally reconstruct the signal properly, in our case, when working at full frame the maximum sampling frequency is 20 Hz, so modulation frequencies must be below 10 Hz [48]. A faster camera would allow for higher sampling frequencies [49]. Several approaches exist for lock-in thermography [5, 13, 50].

The camera used in this work to perform Lock-in thermography is the FLIR SC5000, which has incorporated lock-in possibilities.

1.2.3 Vibrothermography

It means ultrasound excited thermography, thermosonics or sonic infrared. It was first proposed as a thermographic non-destructive evaluation (NDE) technique in the late seventies [51, 52].

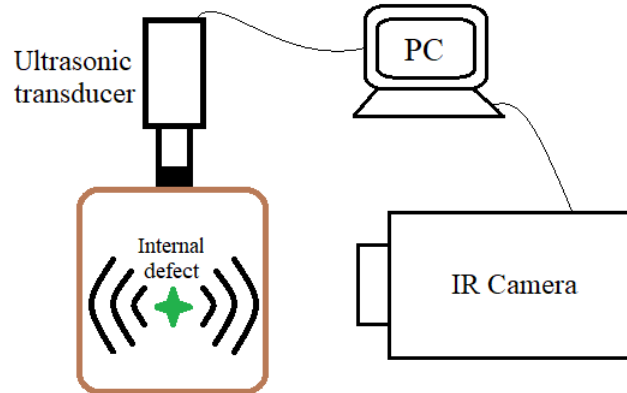


Figure 1.5: Scheme of vibrothermography experiment.

Vibrothermography involves the probing of the internal integrity and uniformity of a sample by observing, through a thermographic camera, the heat pattern produced by the energy dissipation that occurs when a vibrational excitation is applied [53](Fig. 1.5). It consists of a piezoelectric transducer, an optional vibration booster and a sonotrode that is brought into mechanical contact with the test piece in order to induce elastic waves that propagate inside its structure. These three are designed to have the same ultrasonic resonance frequency, typically, 20 or 40 kHz.

At the defects, part of this mechanical energy is dissipated as heat, due to rubbing of the defect's faces or, in the case of cracks, to plastic deformation at the surrounding area [54]. The thermal energy produced at the defects diffuses in the material, producing a temperature rise at the surface that can be measured with an IR videocamera. Given that the detection is based on heat diffusion, vibrothermography is used to detect surface breaking or shallow subsurface defects [17].

Coming to the excitation temporal regimes, vibrothermography has been implemented in basically two schemes: burst and amplitude modulated or lock-in. In burst vibrothermography, short ultrasound pulse (typically from some tens of milliseconds to some seconds) of constant amplitude is applied to the specimen and the evolution of the surface temperature distribution of the sample surface is registered with an infrared camera during and after the excitation. The main advantage of the burst approach is that the experiment is very fast, as the data acquisition takes at most a few seconds.

The presence of the defect can be evaluated in the raw image sequence or, alternatively,

a pulsed phase thermography analysis [55] can be conducted, in which the signal at each pixel is transformed from time domain to frequency domain via the one-dimensional Discrete Fourier Transform (DFT) to extract amplitude and phase at any of the frequencies contained in the burst, which de-noises the data. Phase images are especially interesting as they are less affected than amplitude by emissivity variations, surface orientation and environmental reflections.

2 Influence of convection-radiation heat losses: A thermographic study.

2.1 Introduction

In a previous work [56] a simple phenomenological theoretical model has been developed to account for convection-radiation heat losses (CRHL) in photothermal experiments, whose predictions were compared with the results of measurements using an IR thermometric technique. This study demonstrated that the CRHLs can have a great influence when the condition

$$M = |Z_T| H \ll 1 \tag{2.1}$$

(see next section) is valid, so that they become more important at low modulation frequencies for poor heat conducting materials. Based on the studies carried out, a methodology was proposed for the precise determination of thermal diffusivity. However, due to the lack of phase sensitive detection in the technique used, these experimental studies were reduced to the analysis of the signal amplitude behavior with the modulation frequency, as it was very difficult to detect the signal phase to compare its behavior with that expected following the theoretical model. Here, the IR active lock-in thermographic technique was used to study the influence of CHRL on the phase of the photothermal signal.

2.2 Heat diffusion equation with heat losses: theoretical analysis

In the analysis performed in sec. 1.1.3, the CRHL were not considered in the boundary condition of the problem (Eq. 1.17). If they are present (Fig. 2.1), then Eq. 1.17 must be rewritten as:

$$-k \frac{\partial \Delta T(x, t)}{\partial x} \Big|_{x=0} = \frac{I_0}{2} \text{Re} [1 + e^{i\omega t}] - H \Delta T(0, t) \quad (2.2)$$

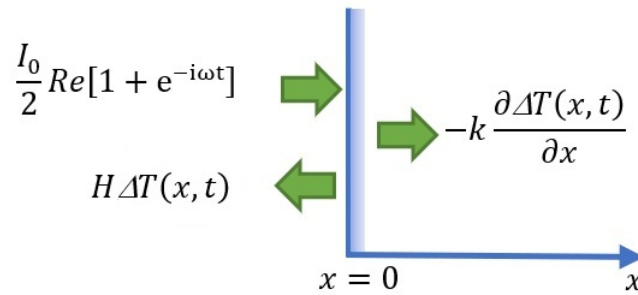


Figure 2.1: Energy balance on the sample surface

It can be demonstrated that using this condition the thermal wave solution becomes:

$$T(x, t) = \frac{I_0 Z_T}{2(1 + Z_T H)} e^{-\frac{x}{\mu}(1+i) - \frac{\pi}{4}} e^{-i\omega t} \quad (2.3)$$

Note that Eq. 1.25 becomes a particular case of Eq. 2.3 when the condition 2.2 is valid.

Therefore, for periodical heating the condition to neglect CRHL respecting conduction is $M \ll 1$. It is easy to see, when compared with Eq. 1.12, that the dimensionless parameter M plays the same role for time variable thermal phenomena that the Biot's number, Bi , does for stationary phenomena. While the later depends on thermal resistance, the M -number is determined by the thermal impedance.

Substituting Z_T in Eq. 2.3 and doing some straightforward calculations Eq. 2.3 takes the form

$$T(x, t) = Ae^{i(\omega t - \phi)} \quad (2.4)$$

where

$$A = \frac{I_o}{2H\sqrt{\frac{2}{M^2} - \frac{2}{M} + 1}} e^{-\frac{x}{\mu}} \quad (2.5)$$

is the amplitude

$$\phi = -\frac{x}{\mu} + \arctan\left(\frac{1}{M-1}\right) \quad (2.6)$$

is the phase, and

$$M = \frac{H}{\epsilon\sqrt{\pi f}} \quad (2.7)$$

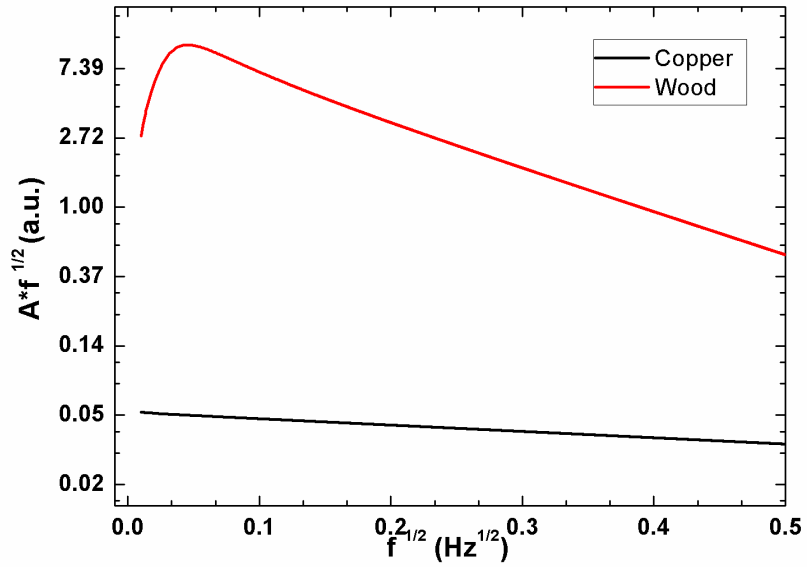
When CRHL are neglected, i.e. when $M \ll 1$, the amplitude and the phase reduce to

$$A|_{M \ll 1} = \frac{I_o}{2\epsilon\sqrt{2\pi f}} e^{-x\sqrt{\frac{\pi f}{\alpha}}} \quad (2.8)$$

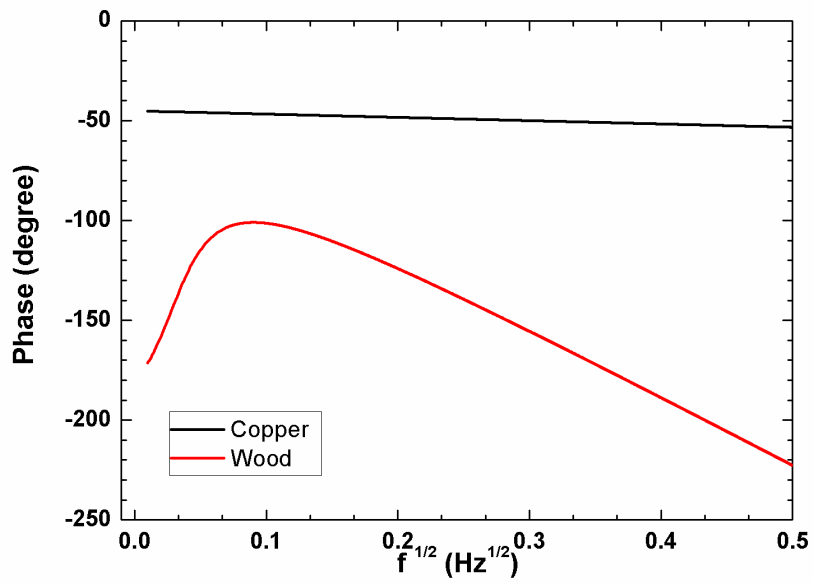
and

$$\phi|_{M \ll 1} = -\frac{x}{\mu} - \frac{\pi}{4} \quad (2.9)$$

respectively. As mentioned in sec.1.1.5, these equations are the basis of the slope method for measurement of the thermal diffusivity, which can be calculated from the slopes ($L\sqrt{\frac{\pi}{\alpha}}$) of the linear graphs $\ln(A\sqrt{f})$ vs. \sqrt{f} and ϕ vs. \sqrt{f} if the amplitude and phase are measured at a well-known distance $x = L$ from the heated region. However, deviations from the linearity are expected due to the presence of the terms containing the parameter M in Eqs. 2.5 and 2.6 due to CRHL.

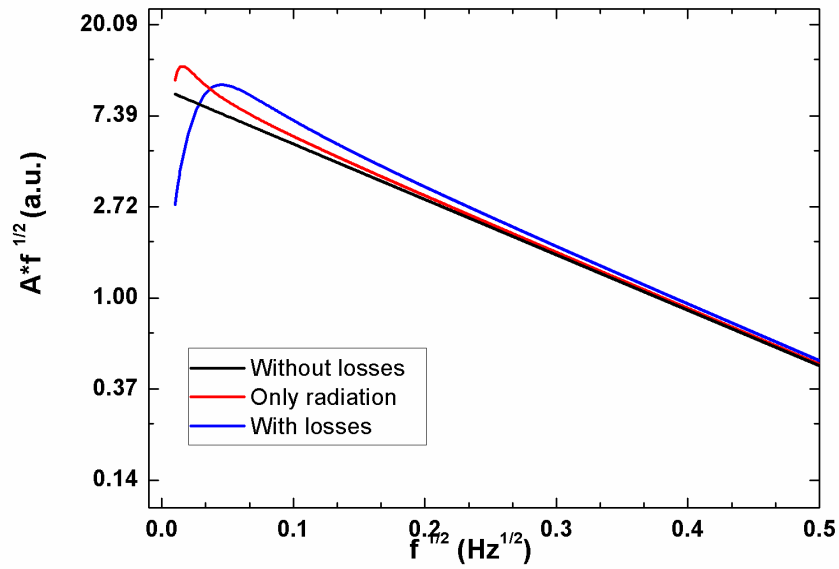


(a)

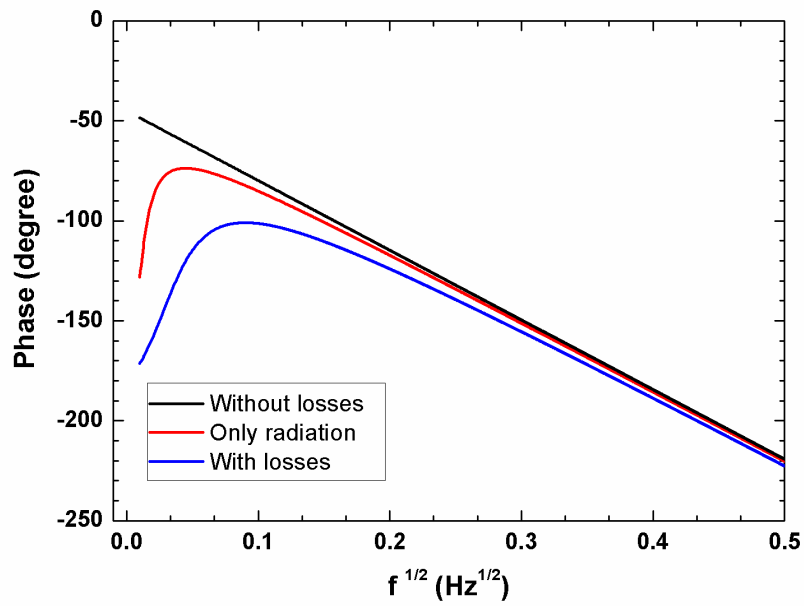


(b)

Figure 2.2: a) $\ln(A\sqrt{f})$ and b) ϕ , as a function of the square root of the modulation frequency for 1 mm thick balsa wood and copper samples.



(a)



(b)

Figure 2.3: a) $\ln(A\sqrt{f})$ and b) ϕ , versus square root of frequency. Simulation of wood when three cases are considered: the radiation heat losses (red), CRHL (blue) and in vacuum (black).

Fig. 2.2 illustrates this situation. They show the results of calculations performed using Eqs. 2.5 and 2.6 for both $\ln(A\sqrt{f})$ and ϕ as a function of the square root of the modulation frequency, \sqrt{f} , for a sample with low (Balsa wood, $\alpha = 2.6 \times 10^{-7} \text{m}^2/\text{s}$, $k = 0.1 \text{W/mK}$) and high thermal conductivity (copper $\alpha = 116 \times 10^{-6} \text{m}^2/\text{s}$, $k = 401 \text{W/mK}$), for $L = 1 \text{mm}$. It was used a typical value $H = 15 \text{W/m}^2$ [26, 57].

It can be seen from the computer simulations that CRHL affect the behavior of the photothermal amplitude and phase channel signals for the low thermal conductivity sample at very low frequencies, while these parameters are not affected for the high thermal conductivity sample. The effects of convective heat losses can be minimized or even eliminated if measurements are performed under high vacuum conditions, but radiation losses are always present. The Fig. 2.3 shows, for the low thermal conductivity sample, also the results of calculations for $h_{\text{conv}} = 0$, i.e. when only radiation losses are present. In this case a value $h_{\text{rad}} = 6 \text{W/m}^2\text{K}$ was used, as given by the Stefan-Boltzmann law for a black body like simple ($\epsilon = 1$) at room temperature $T_0 = 300 \text{K}$. It can be seen that the signals are less affected by radiation losses than by CRHL, but that deviations from the linearity should be expected at low frequencies even when convection is neglected.

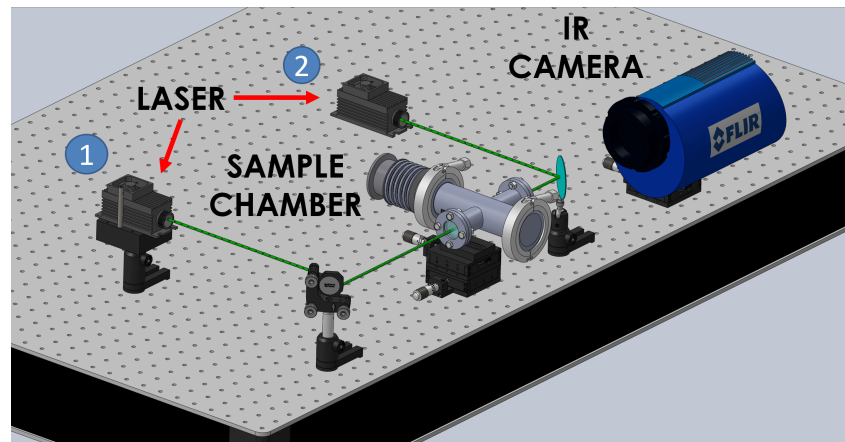
In previous works, the influence of convection and radiation losses on the amplitude of the signal was studied by infrared thermometry [56, 58]. Due to the reasons outlined above, only low thermal conductivity materials have been analyzed in which the effects of CRHL are visible. Because these samples are thermally thick ($\mu \gg L$, where L is the thickness) thermal waves reflection at the rear side of the sample doesn't have any effect on the model developed above for a semi-infinite sample. Here we are going to extend the analysis studying also the CRHL influence on the signal phase. For this, the infrared active lock-in thermography technique will be used.

2.3 Experimental configuration

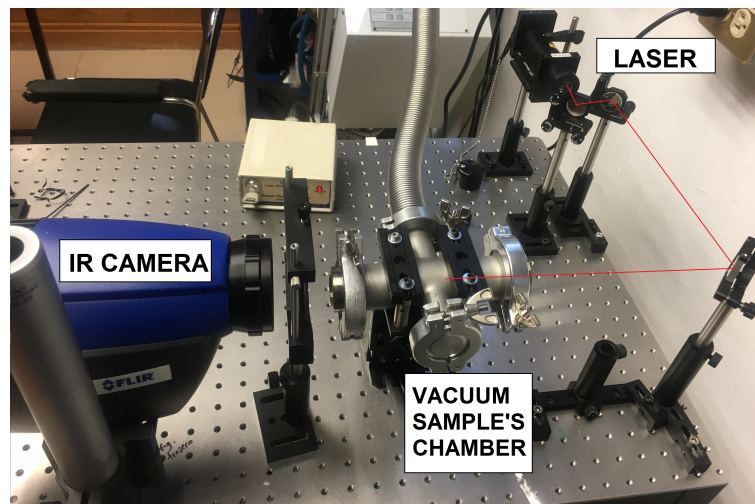
The experimental set-up is shown schematically in Fig. 2.4a, and a photograph is shown in part b of the figure. The sample is located in a vacuum chamber designed to perform measurements under high vacuum conditions and to minimize convection losses. A laser (Lasever INC 12030701, $\lambda=405 \text{ nm}$ and power 300 mW) is TTL-modulated in

2.3 Experimental configuration

amplitude at a frequency, f . The modulated laser beam impinges uniformly on a sample that is previously painted black in order to ensure the superficial absorption of light and an emissivity close to unity. An IR camera (FLIR S5000) interfaced with a personal computer (PC) was used to measure the temperature oscillations resulting at the rear (non-illuminated) surface of the sample. Its main characteristics have been shown in sec.1.2.1. The interface between camera and PC, and the software (IR-NDT) for data acquisition and lock-in data processing used, were provided by the manufacturer.



(a)



(b)

Figure 2.4: a) Schema of the general experimental set-up and b) photo of configuration used.

2.3 Experimental configuration

A germanium window was placed between the IR camera and the sample chamber to prevent laser light incidence on the camera detector. Fig.2.5 shows the optical transmission spectrum of the Ge window. In the experimental arrangement the laser can be switched from position 1 to 2 to allow also measurements in front excitation and detection condition. In this case the Ge window acts also as a mirror to focus the laser beam onto the sample. Both, front and rear configurations have been applied during the course of this thesis work for characterization of several materials systems [58,59].

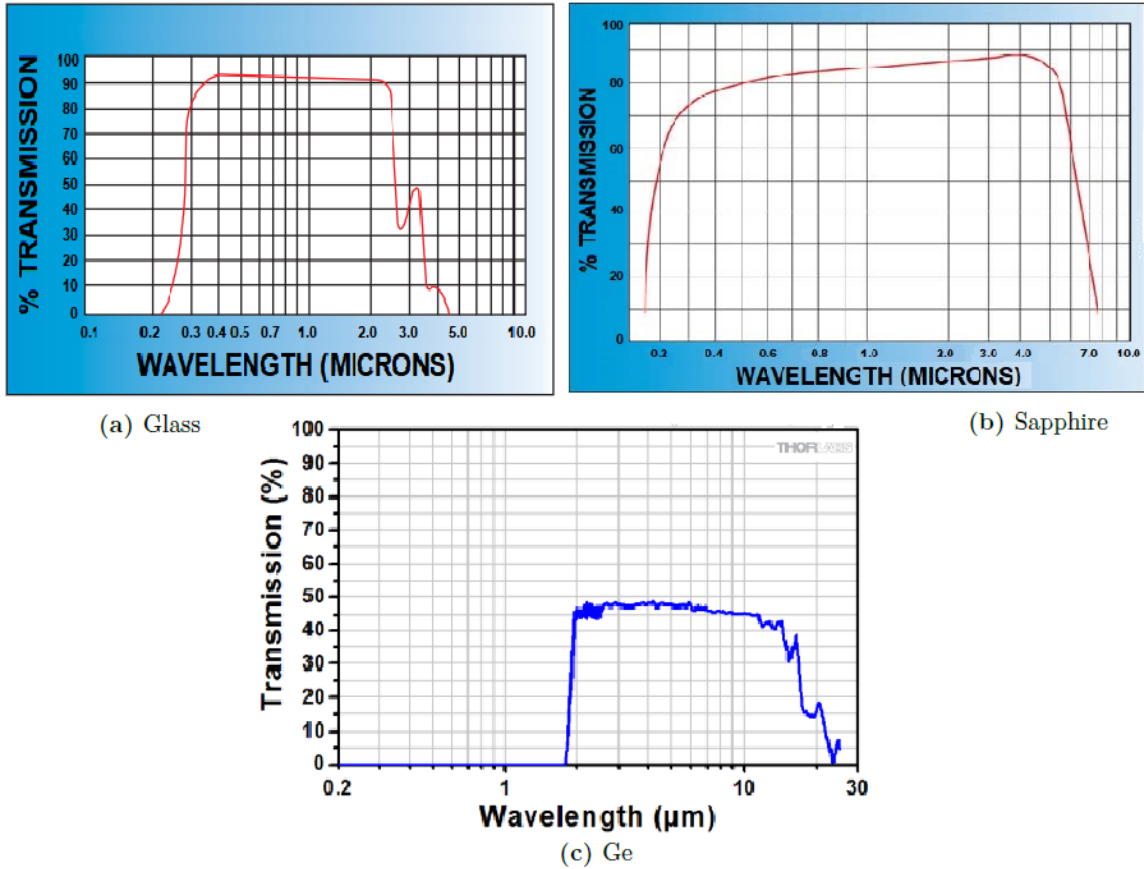


Figure 2.5: Optical Transmission vs. wavelength for the glass, sapphire and Ge windows.

The sample chamber can be kept at high vacuum (1×10^{-7} Torr) during measurement, using a rotatory vacuum pump (Varian Vacuum Technologies, DS 102) coupled to a turbo molecular vacuum pump (Varian Vacuum Technologies, Turbo-V 81-AG). The two pumps are controlled by a control panel (Turbo-V 81-AG Rack Controller) in which

the necessary vacuum for each measurement can be selected. The vacuum chamber was designed in the form of a cross and is shown schematically in Fig. 2.6. It is sealed on the top and bottom using sapphire and glass windows respectively, through which IR radiation propagates to the IR camera and a laser beam is focused to the sample, respectively. Fig. 2.5 also shows the optical transmission spectra of these windows.

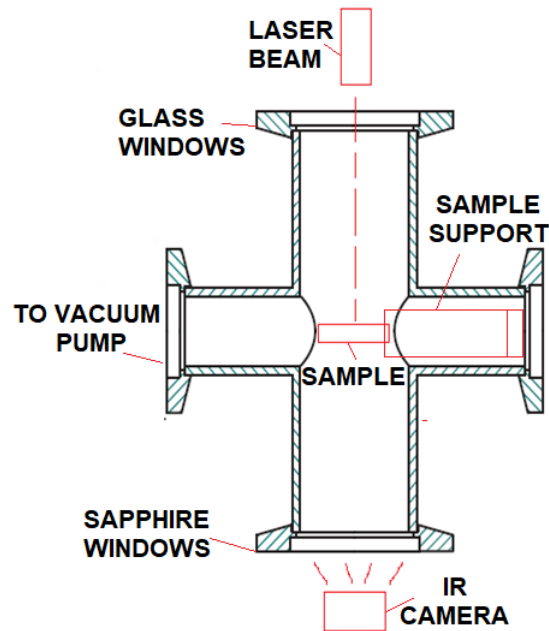
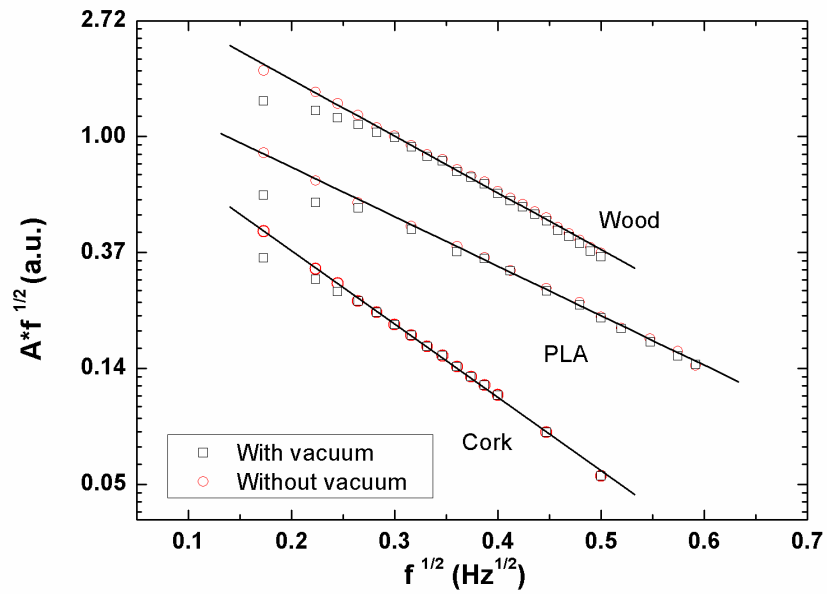


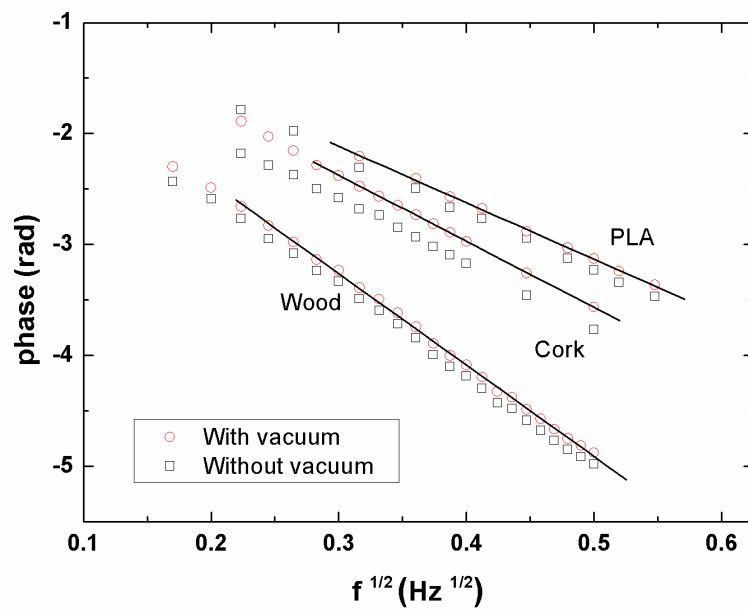
Figure 2.6: Schema of the vacuum sample's chamber.

2.4 Experimental results

Measurements have been performed in balsa wood, cork and plastic samples, whose thicknesses are shown in Tab. 2.1. The amplitude and phase images were collected for each frequencies, between 50mHz and 250mHz at a step of 10 mHz. Typical result are shown in Fig. 2.7. The open circles correspond to measurements performed in vacuum, while squares correspond to measurements without it. Part (a) of the figure shows $A\sqrt{f}$ and part (b) shows the phase as a function of the square root of the modulation frequency.



(a)



(b)

Figure 2.7: a) $A\sqrt{f}$ and b) phase as a function of the square root of the modulation frequency for a balsa wood sample.

Solid curves in the figures are the best least squares linear fits in the frequency region where CRHL can be neglected. From the slopes, m , the thermal diffusivity is calculated as $\alpha = \frac{L^2\pi}{m^2}$. It is worth notice that all solid curves in the phase graphs converge to the awaited $\pi/4$ value when f goes to zero. Tab. 2.1 shows the obtained thermal diffusivities together with literature reported values for comparison, showing a good agreement between them.

		Thickness ($\times 10^{-3}\text{m}$)	Thermal diffusivity ($\times 10^{-7}\text{m}^2/\text{s}$)	Relative uncertainty (%)	α literature ($\times 10^{-7}\text{m}^2/\text{s}$)
Wood	Amp	1.5	2.66 ± 0.12	4	0.82-2.92
	Phase		2.55 ± 0.06	2	
Cork	Amp	1.4	1.50 ± 0.08	5	<1.6
	Phase		1.49 ± 0.09	6	
Plastic PLA	Amp	1.1	1.35 ± 0.03	2	0.6-1.5
	Phase		1.34 ± 0.04	3	

Table 2.1: Results of measurements.

2.5 Conclusions

An experiment was designed and implemented to determine the thermal diffusivity of different materials in high vacuum with an error of less than 5%. It was shown that CRHL become significant at low modulation frequencies for low thermal conductivity materials. It is observed that there is influence of CRHL in the signal phase too. However, taking the linear part where CRHL can be neglected, you can calculate a linear fits and obtain values within the range reported in the literature. The here presented results should be helpful not only for researchers in the field of photothermal techniques, but also for those dealing with any phenomena involving periodical modulated heating of samples.

3 Characterizing of open vertical cracks with burst vibrothermography

3.1 Introduction

In the last decade, the technique of vibrothermography has become of great interest because of its ability to detect defects that are elusive to other NDE techniques. It can be used in a wide variety of materials, and especially, it is very suited and sensitive to the presence of kissing cracks as the relative vibration of the faces produces heat, which diffuses inside the material and can be detected as a temperature variation at its surface by means of an infrared (IR) camera. With the idea of heading for real applications, in this work we focus on burst vibrothermography (VT), and we address the characterization of open cracks. Vibrothermography has turned out to be one of the most suitable and sensitive techniques to detect these defects, with the advantage of having a higher penetration potential than thermographic techniques based on optical excitation.

In a previous work [60], an inversion algorithm was developed, stabilized with a total variation penalty term, to retrieve the size and depth of kissing cracks (which produce compact heat sources) from the thermogram obtained at the end of the burst and the timing-graph corresponding to the central pixel. In this work, open semicircular strip-shaped heat sources were characterized representing open half-penny cracks when the heat is produced at a certain contour, which is closer to a real situation with surface breaking cracks. Moreover, we determine not only the geometry, but also the absolute flux distribution and total power generated at vertical cracks.

In previous works, the identification of the geometry of buried heat sources from VT experiments is tackled, both in modulated [61–65] and burst regimes [60, 66]. It is well

known that the lock-in technique has the potential to reduce the noise in the data by analyzing a large number of images. This allows detecting very weak signals (far lower than the noise equivalent temperature difference (NETD) of the camera) from defects that would remain unnoticed in a live image sequence, but data taking is rather time consuming. In burst regime, the lowest signal that can be detected is limited by the NETD of the camera, but the experiments are fast, which makes it an ideal technique for industrial applications. The situations that we considered in our previous works were kissing vertical cracks, in which heat is produced all along the crack surface, which leads to the generation of compact heat sources. The geometries we analyzed included rectangles, triangles and semicircles, the latter being representative of kissing half-penny cracks. The identification of the geometry of inner heat sources from surface temperature data, which is a severely ill-posed inverse problem, was carried out by regularizing the least square minimization problem, via the addition of penalty terms. With the idea of heading for real applications, in this work we focus on burst VT, and we address the characterization of open cracks. Moreover, by inverting raw data corresponding to the absolute temperature increase at the surface we determine not only the geometry, but also the absolute flux distribution and total power generated at vertical cracks. In open cracks the heat generated at the flaw is not characterized by a compact shape, as heat is not produced along all the crack surface. At the center of the crack, where the lips are not in contact, there is no friction so the heat sources have the shape of a band, corresponding to positions where the lips are both in contact and in relative motion. We take the case of semi-circular stripe-shaped heat sources as representative of the behavior of open surface breaking cracks. First, we consider the case in which the flux is homogeneous within the semi-circular band. As a further step to approach experimental situations with real cracks, we also consider inhomogeneous flux production within the band, analyzing three different situations: angle-, depth- and radius-dependent fluxes. Finally, we present inversions of experimental data obtained on samples with calibrated heat sources activated in VT experiments, both homogeneous and inhomogeneous. With these results, the objective of rapidly characterizing real cracks is promising: it may take only 2 min to locate and characterize the crack area, including the inversion of the data.

3.2 Direct and inverse problems

Direct problem

When a constant amplitude ultrasonic burst of duration τ is applied to the cracked specimen, heat is produced at an area that is smaller than the crack, where the lips are in contact and in relative motion, typically featuring the shape of a band [67]. So, to consider the problem closest to reality, we work with cracks that only emit heat in a certain cut, therefore, the crack is considered as a semicircular band.

Fig. 3.1a shows the geometry of a semi-infinite material contain a planar heat source of arbitrary shape Ω in plane Π ($x = 0$), emitting a constant heat flux $Q(\vec{r})$ during a time interval $[0, \tau]$. Under adiabatic conditions at the surface, the general expression for the surface ($z = 0$) temperature evolution is given by [66, 68]:

$$\begin{aligned}
 T_h(r_{z=0}, t) &= \iint_{\Omega} \frac{Q(\vec{r}')}{2\pi k |r_{z=0} - \vec{r}'|} \operatorname{Erfc} \left[\frac{|r_{z=0} - \vec{r}'|}{\sqrt{4\alpha t}} \right] ds' \quad 0 \leq t \leq \tau \\
 T_c(r_{z=0}, t) &= \iint_{\Omega} \frac{Q(\vec{r}')}{2\pi k |r_{z=0} - \vec{r}'|} \\
 &\quad \left\{ \operatorname{Erfc} \left[\frac{|r_{z=0} - \vec{r}'|}{\sqrt{4\alpha t}} \right] - \operatorname{Erfc} \left[\frac{|r_{z=0} - \vec{r}'|}{\sqrt{4\alpha(t - \tau)}} \right] \right\} ds' \quad t \geq \tau \quad (3.1a)
 \end{aligned}$$

where, k and α are the thermal conductivity and diffusivity of the material, respectively.

In the case we address, the particular geometry of the heat source is a semi-circular band of inner and outer radii r_1 and r_2 , respectively. For the sake of generality, we consider that the upper side is buried at a depth d below the surface (see 3.1b). For this geometry, the evolution of the surface temperature distribution during and after

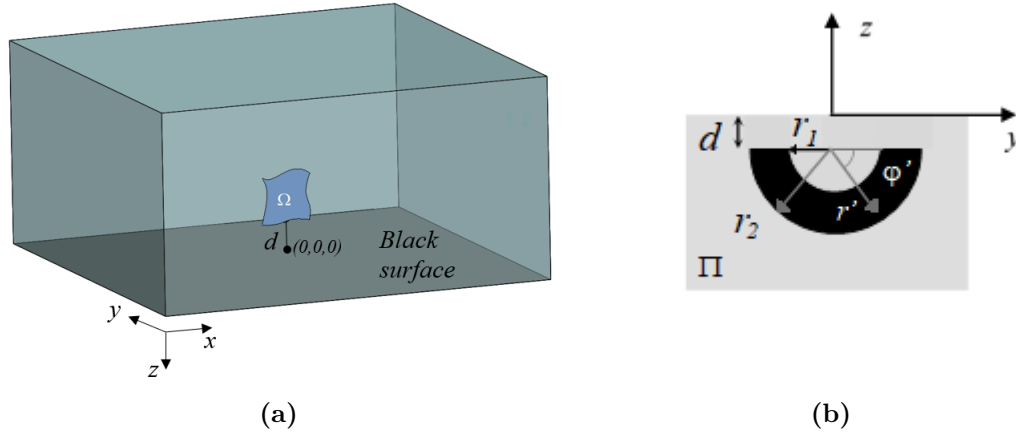


Figure 3.1: Geometry of heat source. a) Heat source of area Ω contained in plane Π ($x = 0$). b) Semi-circular stripe-shaped heat source of inner and outer radii r_1 and r_2 , respectively, buried at a depth d .

the excitation can be expressed as follows:

$$T_h(x, y, 0, t) = \int_{r_1}^{r_2} \int_0^{\pi} \frac{Q(\vec{r}')}{2\pi kL} \operatorname{Erfc} \left[\frac{L}{\sqrt{4\alpha t}} \right] r' dr' d\varphi \quad 0 \leq t \leq \tau \quad (3.2a)$$

$$T_c(x, y, 0, t) = \int_{r_1}^{r_2} \int_0^{\pi} \frac{Q(\vec{r}')}{2\pi kL} \left\{ \operatorname{Erfc} \left[\frac{L}{\sqrt{4\alpha t}} \right] - \operatorname{Erfc} \left[\frac{L}{\sqrt{4\alpha(t - \tau)}} \right] \right\} r' dr' d\varphi \quad t \geq \tau \quad (3.2b)$$

where $L = \sqrt{(y - r' \cos \varphi')^2 + (d + r' \sin \varphi')^2}$. Here, r' and φ' are the planar spherical coordinates, with origin at the center of the semi-circles.

The purpose of our work is to invert surface temperature data to determine not only the geometry but also the absolute flux distribution responsible for the observed temperature, in a fast way. In order to reduce the computational cost of the inversion, we extract selected spatial and temporal information: the thermogram obtained at the end of the burst $T_r = T(x, y, 0, t)$ and the evolution of the temperature at the origin $T_t = T(0, 0, 0, t)$. Note that T_r and T_t , combined in $T = (T_r, T_t)^T$ (superscript T is transpose), represent absolute values of the temperature elevation at the surface, due

to the presence of the crack. Inversion of these raw temperatures will allow us to extract absolute values of the heat flux (and power) emitted by the crack.

Inverse problem

The inverse problem consists in finding the absolute heat flux distribution ($Q(\vec{r})$ in Eqs. 3.2a and 3.2b) responsible for the measured surface temperature. We address the problem without assuming any particular shape of the heat source, only the vertical plane containing the heat sources (easily recognizable from the surface temperature distribution) is taken as prior knowledge. This approach prevents us from addressing the inversion as a parameter estimation problem, in which only the parameters describing a specific geometry are sought. The idea is to mesh the plane that contains the heat sources (plane Π , $x = 0$) and find the heat flux at each node (area element) that minimizes the residual squared R^2 , i.e., the square differences between the noisy data, $T^\delta = (T_r^\delta, T_t^\delta)^T$, and the calculated temperatures:

$$R^2 = \|T_{\text{calc}}(Q^\delta) - T^\delta\|^2 \quad (3.3)$$

where the noise level is defined as $\delta^2 = \|T^\delta - T\|^2$, being $\|g\|^2 = \iint_{z=0} g^2(x, y) dx dy$, and Q^δ is the retrieved flux distribution from noisy data.

The minimization of R^2 in Eq. 3.3 involves the determination of a large number of parameters (equal to the number of nodes used to mesh plane Π). Given the diffusive nature of heat propagation, the inverse problem is severely ill-posed and the minimization of the residual in Eq 3.3 requires regularization. The stabilization can be carried out by adding regularization terms based on Tikhonov (TK_0) [69], Total Variation (TV) [70], and Lasso (L_1) [71] functionals, defined as:

$$TK_0(Q) = \iint_{\Pi} |Q|^2 ds \quad (3.4)$$

$$TV(Q) = \iint_{\Pi} |\nabla Q| ds \quad (3.5)$$

$$L_1(Q) = \iint_{\Pi} |Q| ds \quad (3.6)$$

Based on these penalty terms, the new residual to be minimized writes:

$$R_{\alpha^i}^2 = \alpha_{TK}^i TK_0 \left(Q_{\alpha^i}^{\delta, r} \right) + \alpha_{TV}^i TV \left(Q_{\alpha^i}^{\delta, r} \right) + \alpha_{L_1}^i L_1 \left(Q_{\alpha^i}^{\delta, r} \right) + \left\| T_{calc} \left(Q_{\alpha^i}^{\delta, r} \right) - T^\delta \right\|^2 \quad (3.7)$$

Here each functional is multiplied by a regularization parameter that determines the relevance of the stabilizing term with respect to the discrepancy term (last term on the right hand side of Eq 3.7). Finding the appropriate values of the regularization parameters is a sensitive issue: they should be high enough to actually stabilize the inversion and, at the same time, as small as possible in order to introduce the smallest error. Our strategy is to start with rather high values of the regularization parameters and reduce them in successive iterations (for details regarding the inversion algorithm see [60]). Obviously, the addition of these penalty terms affects the retrieved solution $Q_{\alpha^i}^{\delta, r}$ (here $r = (\alpha_{TK}^i, \alpha_{TV}^i, \alpha_{L_1}^i)$ represents the combination of the three regularization parameters). When applying this methodology, the key point is an appropriate determination of the value of r , when iterations are stopped. For the sake of clarity, in the following we denote the final reconstructed heat flux $Q_{\alpha^i}^{\delta, r} = Q_R$. In inversions of synthetic data affected by a given (and accurately known) noise level, applying the Morozov stopping criterion gives excellent results: it consists in stopping iterations when the discrepancy term is of the order of the noise in the data [72]. In inversions of experimental data, on the contrary, the noise level is an uncertain quantity: in addition to the random noise associated to the temperature measurement, data might also be affected by systematic (and unknown) errors. For this reason, the application of the Morozov criterion to experimental data is tricky.

3.3 Inversion of synthetic data

In this section we analyze the performance of the algorithm by inverting synthetic data calculated for AISI 304 stainless steel ($k = 16\text{W/mK}$, $\alpha = 4\text{mm}^2/\text{s}$), which is the material our samples are made of. First, we analyze the case of semi-circular, stripe-shaped heat sources emitting a homogeneous flux. Eqs. 3.2a and 3.2b have been computed to generate surface temperature data for a semicircular band of inner

and outer radii $r_1 = 1\text{mm}$ and $r_2 = 2\text{mm}$, respectively, buried at a depth $d = 0.1\text{mm}$ and emitting a homogeneous flux of $Q = 5 \times 10^4\text{W/m}^2$, which corresponds to a total emitted power of $P_E = 0.234\text{W}$. Its 3D geometry is given in Fig. 3.2a). The effect of changing the radii, the burst duration and the noise level in the data will be analyzed in the following.

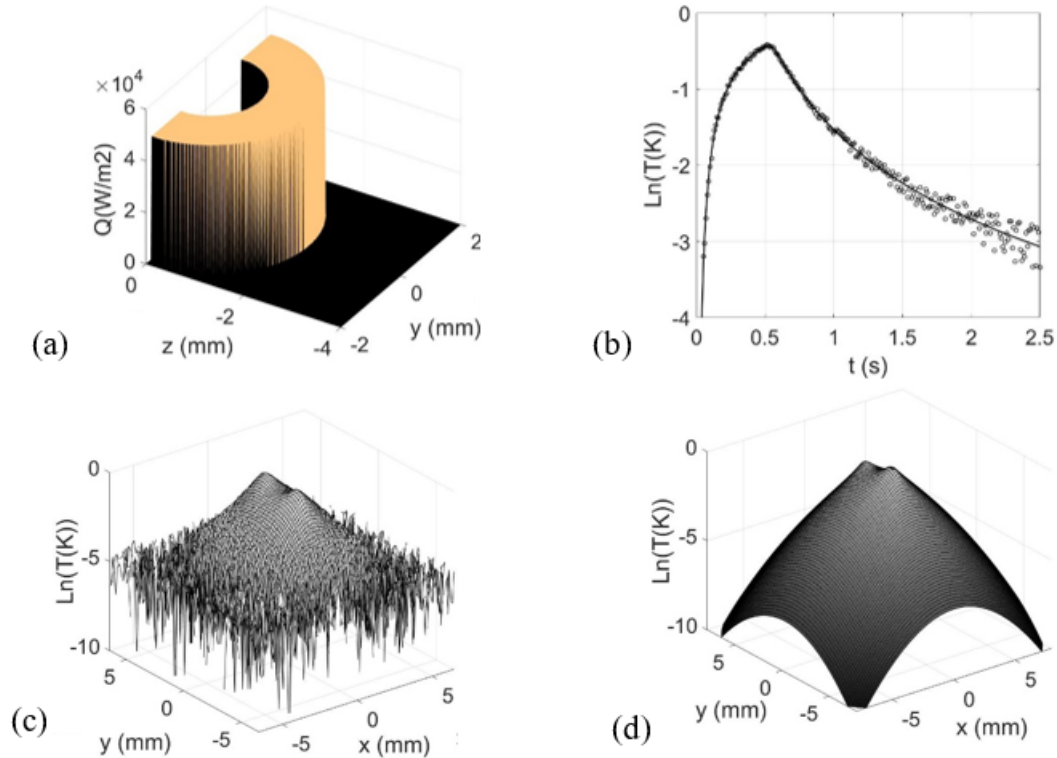


Figure 3.2: a) 3D representation of a semi-circular stripe-shaped heat source of inner and outer radii $r_1 = 1\text{mm}$ and $r_2 = 2\text{mm}$, respectively, buried at a depth $d = 0.1\text{mm}$ and emitting a homogeneous flux . b) Noisy (5%, symbols) and fitted (solid line) T_t at the central pixel. c) and d) Noisy (5%) and b) fitted T_r , obtained at the end of $\tau = 0.5\text{s}$.

3.3.1 Effect of burst duration

We have tested three burst durations: $\tau = 0.5, 3$ and 8s . In all cases, a 5% random noise, which is similar to that found in VT experiments, have been added. Fig. 3.2(b)

shows the noisy and fitted temperature evolution at the central pixel, T_t , (symbols and solid line, respectively) corresponding to a burst duration of $\tau = 0.5s$. Fig. 3.2(c) and (d) show the noisy and fitted thermograms T_r calculated at the end of the burst, respectively, for the same burst duration.

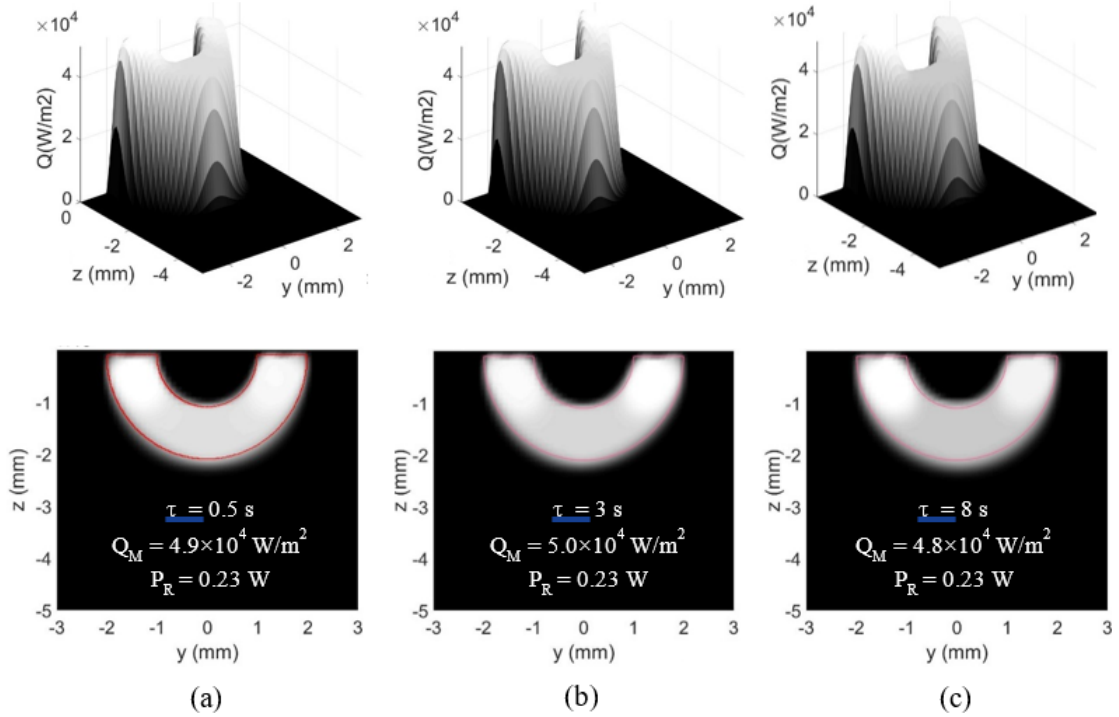


Figure 3.3: Top: 3D representation of the retrieved absolute heat flux distribution, $Q_R(\vec{r})$, corresponding to the real heat source depicted in Fig. 1.2 (d) ($r_1 = 1mm$, $r_2 = 2mm$, $d = 0.1mm$, $PE = 0.234W$), obtained from synthetic data corresponding to burst durations of (a) $\tau = 0.5s$, (b) $\tau = 3s$, and (c) $\tau = 8s$, and data affected by 5% noise. Bottom: 2D gray level representation of the normalized heat source distributions, Q_N . The red lines represent the real contours of the heat sources. The retrieved maximum flux Q_M and total power P_R are displayed on each reconstruction.

The reconstructions for the three burst durations are depicted in Fig. 3.3. On top, we present 3D images of the retrieved absolute heat flux distributions, $Q_R(\vec{r})$. In order to better visualize the geometry of the heat sources, at the bottom we display a 2D grey level representations of the normalized heat flux distribution $Q_N(\vec{r})$, which is defined as $Q_N(\vec{r}) = \frac{Q_R(\vec{r})}{Q_M}$, where Q_M is the maximum value of the retrieved heat flux. White represents $Q_N(\vec{r}) = 1$ and black $Q_N(\vec{r}) = 0$. The values of Q_M and the total retrieved

power, P_R , are also specified for each reconstruction. As can be observed, not only the geometry of the heat sources is well identified, but also the absolute values of the flux and emitted power are retrieved very accurately. Note that the quality of the reconstructions is rather independent of the duration of the burst.

However, if we reduce the thickness of the stripe down to $400\mu\text{m}$ ($r_1 = 1\text{mm}, r_2 = 1.4\text{mm}, d = 0.1\text{mm}$) while keeping the heat flux $Q = 5 \times 10^4\text{W}/\text{m}^2$ (i.e. $P_E = 0.075\text{W}$) and the 5% noise level in the data, the influence of the burst duration on the quality of the reconstruction is more noticeable. As can be observed in Fig. 3.4, a short ($\tau = 0.5\text{s}$) burst that carries a relatively larger high frequency content provides better definition of narrow features than a long burst ($\tau = 5\text{s}$). The reconstructions from long bursts exhibit a shadowing effect: the shallow tips appear brighter and sharper than the deep central side. However, the total retrieved power is rather accurate, the fainter local flux at the deepest side being compensated by the reconstruction overflowing the real contour.

3.3.2 Effect of noise level

We have also checked the influence of the noise level in the data on the retrieved heat fluxes. In Fig. 3.5 we present reconstructions corresponding to the same heat source depicted in Fig. 3.2a) ($r_1 = 1\text{mm}, r_2 = 2\text{mm}, d = 0.1\text{mm}, Q = 5 \times 10^4\text{W}/\text{m}^2, P_E = 0.234\text{W}$) obtained from synthetic data calculated for a burst duration of $\tau = 2\text{s}$, affected by three noise levels: 0.5, 5 and 10%.

The results in Fig. 3.5 demonstrate that the noise level in the data affects both the distribution of the flux and the maximum flux value: the larger the noise level, the more pronounced the shadowing effect, meaning that the retrieved heat sources spread over an area larger than the real area they occupy. However, the shadowing effect does not affect the retrieved total emitted power, which is identified very accurately even for data affected by 10% noise.

3.3.3 Non-homogeneous heat sources

The results displayed in Fig. 3.3 to Fig. 3.5 correspond to homogeneous heat sources. However, in experiments with real cracked samples, the heat distributions generated

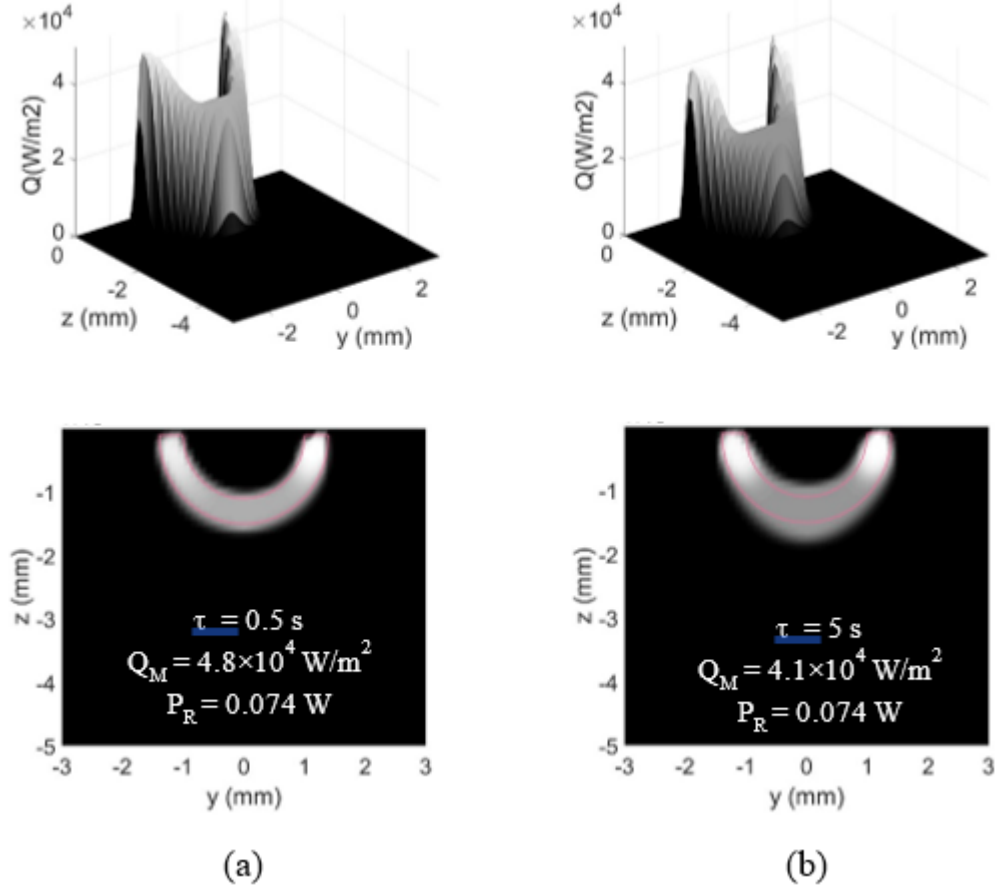


Figure 3.4: The same as in Figure 3.3 but for a narrower heat source of radii $r_1 = 1\text{mm}$ and $r_2 = 1.4\text{mm}$, buried at the same depth $d = 0.1\text{mm}$, and emitting the same homogeneous flux of (i.e. $P_E = 0.075\text{W}$). Reconstructions obtained for: (a) $\tau = 0.5\text{s}$ and (b) $\tau = 5\text{s}$

at cracks are very likely inhomogeneous. In order to mimic the conditions we have tried to implement in experiments with calibrated inhomogeneous heat sources, we next consider the case of semi-circular stripe-shaped heat sources ($r_1 = 1\text{mm}$ and $r_2 = 2\text{mm}$, $d = 0.1\text{mm}$) divided vertically into two equal quarters, each one emitting a homogeneous (but different) flux. We present three cases in which the heat flux emitted by the left quarter (A) remains fixed $Q_A = 5 \times 10^4\text{W/m}^2$ while the right quarter (B) emission varies: $Q_B = 1.25 \times 10^4$, 2.5×10^4 and $3.75 \times 10^4\text{W/m}^2$. In Fig. 3.6 we present the 2D grey level representations of the normalized heat flux distributions obtained from synthetic data calculated for a $\tau = 1\text{s}$ burst, affected by 5% noise.

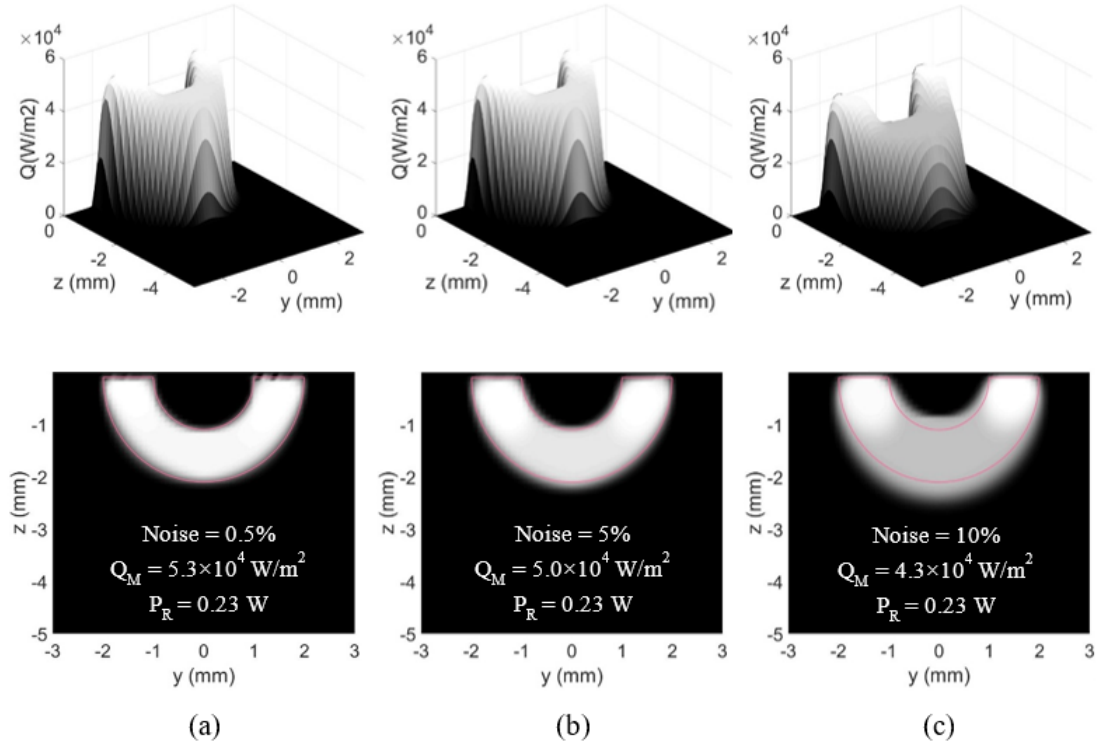


Figure 3.5: The same heat source as in Figura 3.3, but for a burst duration of $\tau = 2\text{s}$. Three noise levels are considered: (a) 0.5% and (b) 5% and (c) 10%

As can be seen, the reconstructions give good geometrical representations of the two homogeneous quarters, as well as very accurate values of the absolute fluxes and powers in all cases. This result indicates the adequacy of the penalty terms selected to stabilize the inversion.

In order to further approach real situations in VT experiments with open cracks, in the following we consider three different continuously varying fluxes within semi-circular stripe-shaped heat sources of radii $r_1 = 1\text{mm}$, $r_2 = 2\text{mm}$ and depth $d = 0.1\text{mm}$, namely, depth-, angle- and radius-varying fluxes. The 2D grey level representations of the normalized reconstructions are displayed in Fig. 3.7. In all cases, the temperature data for the inversions were calculated for $\tau = 1\text{s}$ and for fluxes varying linearly from 0 to $5 \times 10^4 \text{ W/m}^2$ as a function of the corresponding spatial coordinate (lower figures). For each distribution, we display reconstructions obtained by inverting data with two noise levels: 1% and 5%. The nominal and retrieved maximum flux and total power are summarized in Tab. 3.1.

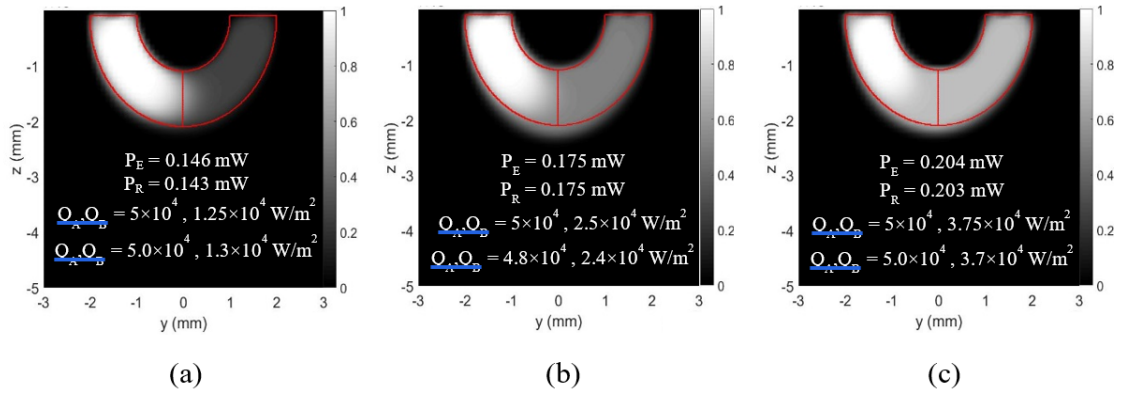


Figure 3.6: 2D grey level reconstructions obtained for semi-circular stripe-shaped heat sources ($r_1 = 1\text{mm}$ and $r_2 = 2\text{mm}$, $d = 0.1\text{mm}$) divided into two quarters. The heat flux on the left is fixed $Q_A = 5 \times 10^4 \text{W/m}^2$ while heat fluxes on the right vary: (a) $Q_B = 1.25 \times 10^4 \text{W/m}^2$, (b) $Q_B = 2.5 \times 10^4 \text{W/m}^2$ and (c) $Q_B = 3.75 \times 10^4 \text{W/m}^2$. The third row corresponds to the nominal heat fluxes, while the fourth one stands for the retrieved fluxes at the homogeneous zones of the reconstructions.

Inspection of Fig. 3.7 shows that, although the radius dependent flux is hard to characterize, the geometrical variation of the depth-dependent flux is in qualitative good agreement with the true flux and that the identification of the angle-dependent flux is really accurate. This indicates that the algorithm is able to identify smooth flux variation as opposed to large gradients, the performance being better if the variation is quasi-parallel to the surface, rather than in depth.

On the other hand, the results also show that the quality of the reconstructions depends largely on the noise in the data so, in order to precisely identify inhomogeneous fluxes, a low noise level in the data is highly desirable. Regarding the absolute values of the retrieved fluxes, the coincidence with the nominal values is not that accurate, but once again, the coincidence between the nominal and retrieved total power is excellent.

These results point out to an outstanding ability of the proposed method to identify the thermal power emitted by a vertical crack in VT experiments. Moreover, the geometry of the heat flux and the absolute values of the heat flux distribution can be determined very accurately for blocky-type flux distributions. The method reaches its limits when it comes to identify large continuously varying flux gradients, but the reconstructions of smooth flux variations are noticeably accurate.

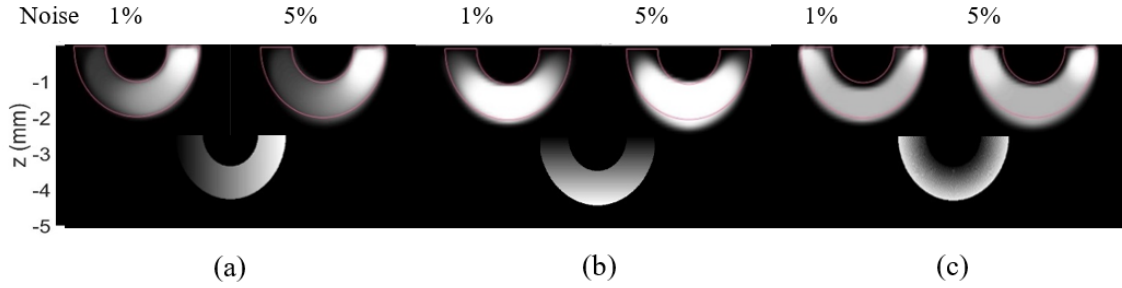


Figure 3.7: 2D grey level representation of the normalized heat flux distribution, $Q_N(\vec{r})$, corresponding to heat sources of the same shape ($r_1 = 1\text{mm}$, $r_2 = 2\text{mm}$ and $d = 0.1\text{mm}$) emitting linear (a) angle-dependent, (b) depth-dependent, and (c) radius-dependent fluxes, obtained from synthetic data corresponding to a burst duration of $\tau = 1\text{s}$ and noise levels of 1% and 5%. The last row corresponds to the real heat flux distribution.

3.4 Experiments and inversion of experimental data

The measurements presented below were made in the photothermal techniques laboratories of the Universidad del País Vasco (UPV), Bilbao, Spain. In order to test the method with experimental data, we need to prepare samples that generate calibrated inner heat sources when excited with ultrasounds. The preparation of the samples is intended to produce a homogeneous heat flux. They basically consist of two identical parts, made of AISI 304 stainless steel, featuring perfectly matching, well rectified flat surfaces [73]. A diagram of the samples is depicted in Figure 3.8a. We put a Cu slab, $37\ \mu\text{m}$ thick, of known dimensions between the two flat surfaces, and we attach the two parts with screws. When we launch the ultrasounds there is friction between the Cu slab and the steel surfaces, so the Cu slab becomes a heat source. We also place two more Cu slabs of the same thickness at the back side of the flat surfaces, to guarantee that they are parallel. These additional Cu slabs are located far enough from the surface where data are taken, so that they do not disturb the surface temperature distribution generated by the calibrated slab. The parallelism of the two steel parts guarantees a homogeneous heat flux along the surface of the Cu slab.

The vibrothermography setup is shown in Figure 3.8b. We use a tunable (15-25 kHz) ultrasound equipment from Edevis with a maximum power of 2 kW (at 20 kHz), and we excite the sample at a single ultrasound frequency of 22.9 kHz. The sample is excited

3.4 Experiments and inversion of experimental data

	Angle dependence		Depth dependence		Radius dependence	
Noise level (%)	1	5	1	5	1	5
Nominal $Q_M(\text{W}/\text{m}^2)$	5×10^4		5×10^4		5×10^4	
Retrieved $Q_R(\text{W}/\text{m}^2)$	4.7×10^4	4.4×10^4	3.0×10^4	2.5×10^4	3.7×10^4	3.2×10^4
Nominal $P_E(\text{W})$	0.120		0.104		0.130	
Retrieved $P_R(\text{W})$	0.118	0.118	0.102	0.103	0.128	0.129

Table 3.1: Nominal and retrieved values of the maximum flux and power corresponding to the reconstructions depicted in Figure 3.7.

with constant power bursts ranging from 0.5 to 3.5 s, and ultrasound electrical powers ranging between 60 and 120 W. The sample surface is covered with high emissivity paint. A thin aluminum film is inserted between the sample and the sonotrode to favor the injection of the ultrasounds in the sample. We capture the radiation coming from the sample surface with an infrared video camera (JADE, J550M from Cedip), working in the 3.5 to 5 m range, equipped with a 320 x 240 detector and a 50 mm focal length lens. In each film, the first frame is subtracted to obtain the temperature rise above the ambient and to compensate for eventual emissivity inhomogeneities.

It should be noted that before starting the measurements, some basic measurements of compact cracks were made (rectangles), thus ensuring that measurements were being made correctly. The pressure that the two screws make to join the two parts of the sample is important 3.8a, it must be ensured that it is not too fixed: otherwise, the vibration will not be generated as it should be. And not so weak because it would not generate vibration.

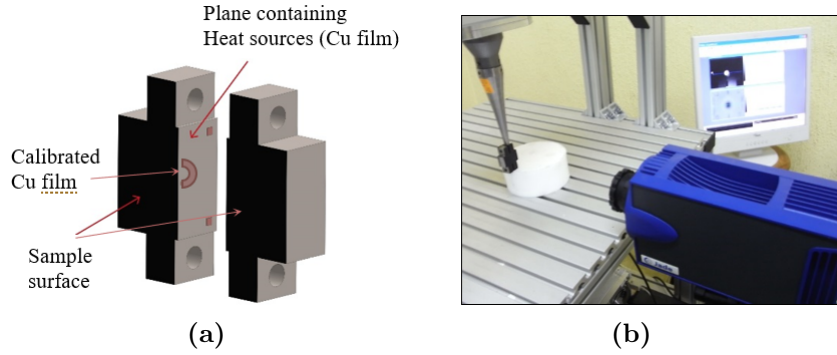


Figure 3.8: Scheme of the experiment. a) Diagram of the samples containing the Cu films. b) Picture of the setup with the sample in place for excitation.

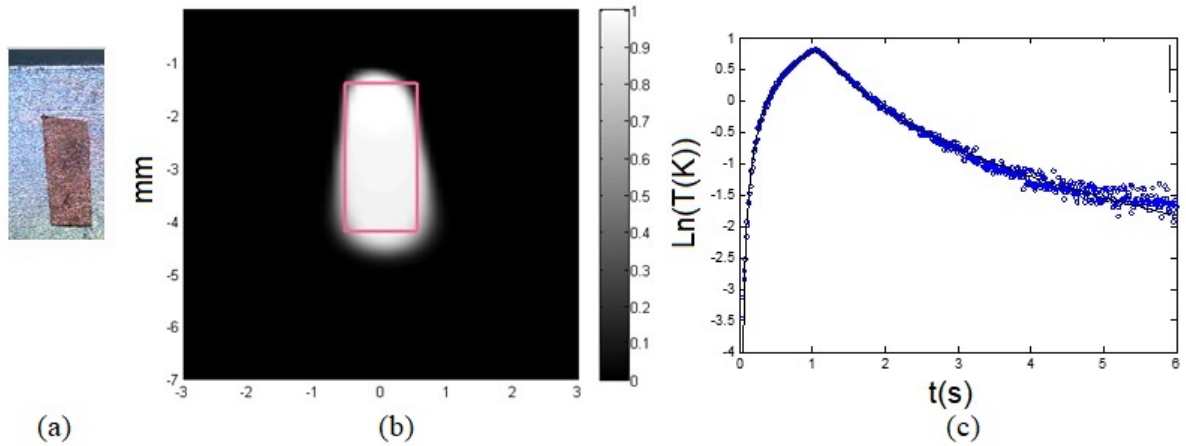


Figure 3.9: a) optical image. b) reconstruction of experimental data obtained for a rectangular at a depth of $d = 0.15\text{mm}$ showed at the left in the micrograph. c) Experimental (symbols) and fitted (solid line) timing graph measured at the central pixel.

In the Fig.3.9 is observed that it is a good reconstruction despite being at a large distance from the surface. Despite its base be at a distance $d = 1.3\text{ mm}$ and its height is 3 mm , the algorithm manages to reconstruct the image.

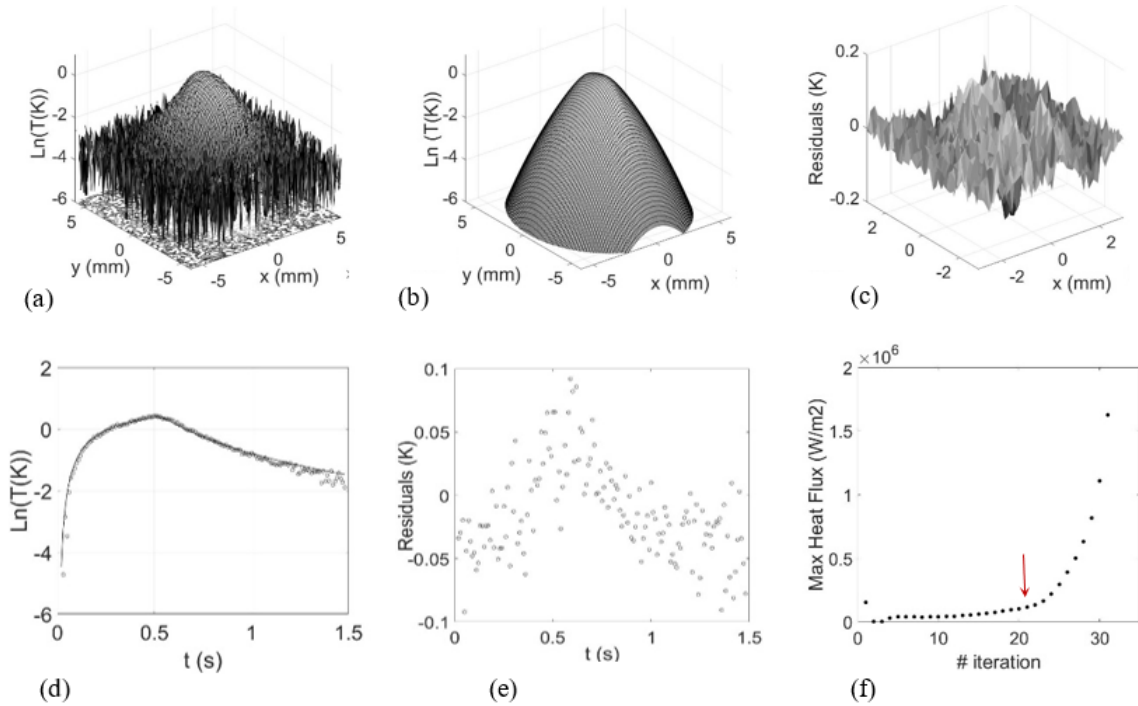


Figure 3.10: a) Experimental thermogram obtained at the end of a burst of $\tau = 0.5$ s, for a semi-circular Cu band on radii $r_1 = 1.2$ mm, $r_2 = 2.1$ mm buried at a depth of $d = 0.15$ mm. b) Fitted thermogram and c) residuals of the thermogram. d) Experimental (symbols) and fitted (solid line) timing graph measured at the central pixel, and e) residuals of the timing graph. f) Evolution of the maximum flux along the iteration process. The red arrow indicates the iteration where the process was stopped.

Next, reconstructions of defects that simulate open cracks will be shown. We took data on samples containing calibrated Cu slabs of different geometries and dimensions, on which we applied bursts of different durations. As an example, in Fig.3.10 we show experimental T_r and T_t data together with the fittings, the residuals, and the evolution of the maximum heat flux distribution Q_M retrieved along the iteration process, for a semi-circular Cu band of radii $r_1 = 1.2$ mm, $r_2 = 2.1$ mm buried at a depth of $d = 0.15$ mm, excited with a burst duration of $\tau = 0.5$ s. In order to apply the Morozov stopping criterion (which is based on knowledge of the noise in the data) to experimental data, an accurate determination of the noise level in the data is necessary. This is not easy to accomplish with experimental data. Accordingly, we have sought an alternative, phenomenological stopping criterion. We have looked

at the maximum retrieved flux along the iteration process Q_M and we have found that the evolution of this quantity features a disruption at the iteration that provides the optimum reconstruction (see Fig. 3.10f)). After this iteration, the maximum flux increases at a rate much larger than the rate in previous iterations, and the area of the reconstructed flux shrinks very fast and features spikes.

This is indicative of the minimization becoming unstable due to very low values of the regularization parameters in Eq. 3.7. The reconstructions depicted in Fig. 3.10 have been obtained by stopping the iteration process at iteration no. 21. This stopping criterion has been applied in all the following experimental reconstructions.

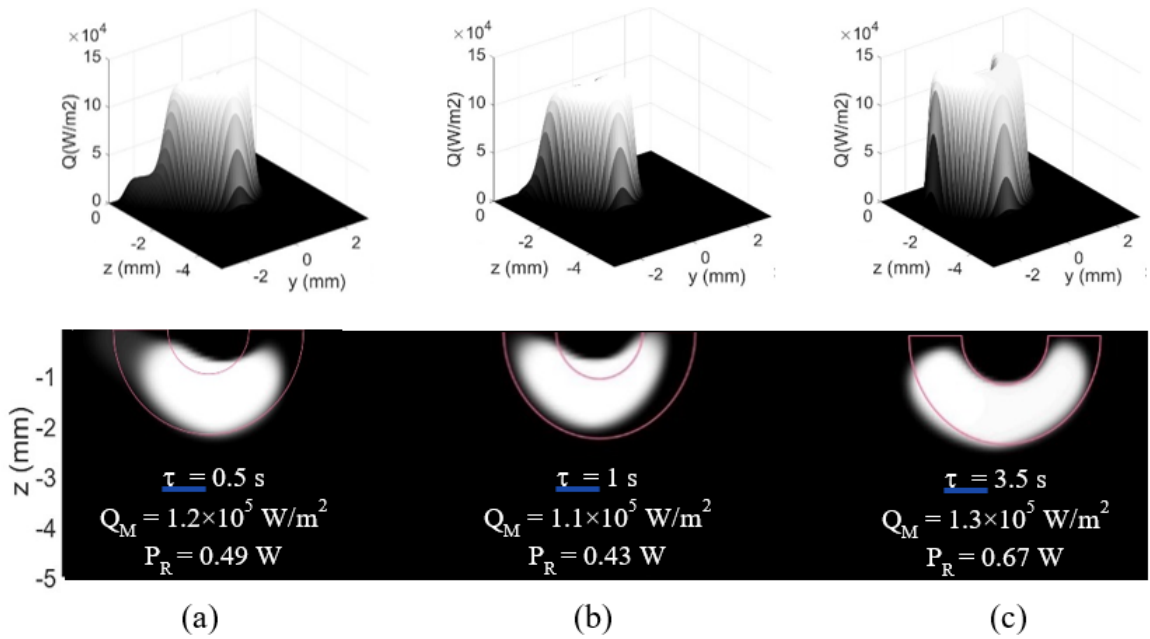


Figure 3.11: Top: 3D representations of the heat flux distributions retrieved for a semi-circular Cu band of radii $r_1 = 1.2\text{mm}$, $r_2 = 2.1\text{mm}$ buried at a depth of $d = 0.15\text{mm}$, excited with three burst durations: a) $\tau = 0.5\text{s}$, b) $\tau = 0.5\text{s}$ and c) $\tau = 0.5\text{s}$. Bottom: 2D grey level representation of the normalized heat flux distributions.

As can be observed in Fig. 3.10, the quality of the fittings is quite good. The residuals in the thermogram (Fig. 3.10c)) are random, and limited to 0.1 K. The residuals in the timing graph (Fig. 3.10e)) are also essentially random and below 0.1 K. The maximum temperature rise in this data set is 1.5 K, so the residuals are below 10%. The 3D representation of the retrieved flux distribution $Q_R(\vec{r})$ and the grey level representation

of the normalized heat flux distribution $Q_N(\vec{r})$ retrieved from the inversion are depicted in Fig. 3.11a). In Fig. 3.11b) and Fig. 3.11c) we represent the reconstructions obtained for the same Cu slab and longer bursts: 1 and 3.5 s. The maximum flux and total power retrieved from the fittings are also written on each reconstruction.

The ultrasounds were applied with the same electrical power of 60W in all cases. Although we do not have reference values for the emitted flux and power, we obtain consistent values of the retrieved maximum flux and total power in the three cases, although the values increase slightly with the (b), (a), (c) sequence. It is worth mentioning that the sequence of data taking was also (b), (a), (c). The increase in the retrieved maximum flux and total power might be associated to variations in the tightening of the screws joining the two steel parts together during the excitation process. We also took data on samples containing Cu slabs of other dimensions and geometries, and buried at different depths. The reconstructions are depicted in Fig. 3.12, together with the retrieved values of the maximum flux and total power, and the micrographs of the Cu slabs used to take data.

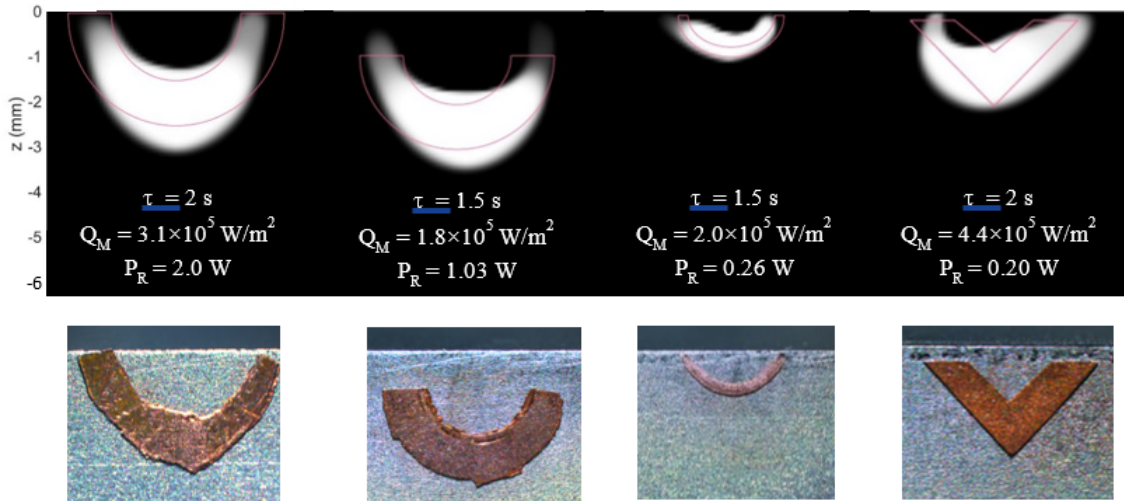


Figure 3.12: Top: reconstruction of experimental data obtained with Cu slabs of the geometry indicated by the red line, for different burst durations. The retrieved maximum flux and total power on each reconstruction. Bottom: micrographs of the Cu slabs used to take data.

Finally, we tried to conduct an experiment with an inhomogeneous heat source. Generating a continuously varying and calibrated flux is very challenging in VT experiments.

Given that our samples are intended to produce a homogeneous flux over the area of the Cu slab, we decided to use Cu films with different treatments to generate homogeneous (but different) fluxes within both slabs: one of the sheets was made of annealed Cu and the other of hard Cu. We took data on a sample containing two Cu bands with an approximate shape of a quarter of a cycle each made of one type of film (see a micrograph of the Cu slabs on the steel surface in Fig. 3.13a). In Fig. 3.13b) and c) we show the 2D grey level representation of the normalized heat flux distribution $Q_N(\vec{r})$ and the 3D representation of the retrieved heat flux distribution $Q_R(\vec{r})$, respectively. As can be seen, the reconstruction exhibits two different areas with almost homogeneous flux, which roughly correspond to the areas of the two Cu slab quarters. The values of the fluxes retrieved at the two green dots depicted in Fig. 3.13c) with denominations A and B are $Q_A = 1.9 \times 10^4(\text{W}/\text{m}^2)$ and $Q_B = 1.4 \times 10^4(\text{W}/\text{m}^2)$, respectively. The retrieved total emitted power is $P_R = 0.523(\text{W})$. Once again, we do not have an independent estimation of the real flux, but the small difference between the fluxes on both sides is plausible, as we obtained the data with two slabs of the same material but slightly different surface condition.

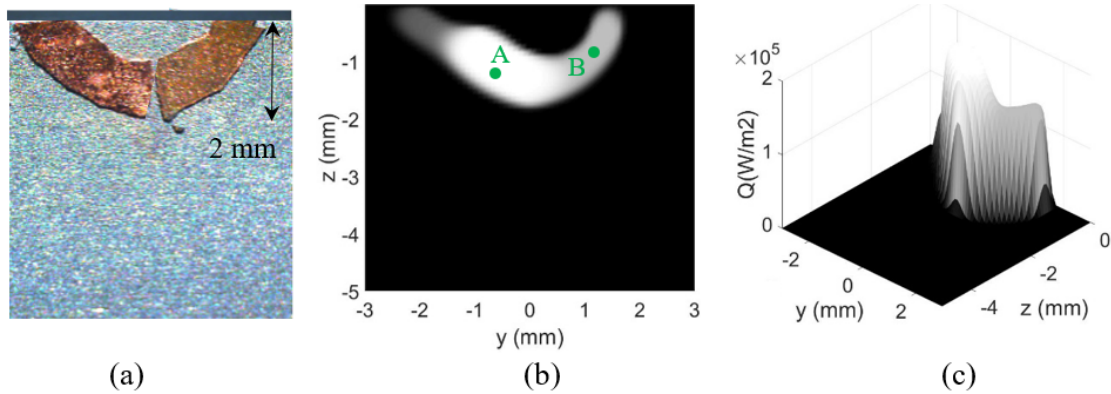


Figure 3.13: a) Micrograph of the two Cu slabs used to produce an inhomogeneous heat flux. b) 2D grey-level representation of the normalized heat flux distribution $Q_N(\vec{r})$ and c) 3D representation of the retrieved flux distribution $Q_R(\vec{r})$ for $\tau = 2\text{s}$.

3.5 Conclusions

The results of this chapter show that it is possible to determine the geometry of heat sources, i.e., inversions of synthetic data with added uniform noise indicate that the flux distribution is retrieved very accurately in the cases of homogeneous and step-shaped fluxes. Continuously varying fluxes can be characterized if the gradient is not large and occurs preferably in the direction parallel to the surface, but the total emitted power is retrieved very accurately, regardless of the specific spatial dependence. The experiments performed on samples containing geometrically calibrated heat sources provide results that seem consistent, even if there are not references for absolute fluxes and emitted powers. The methodology is also applicable to kissing cracks producing compact heat sources. We believe that this approach, which allows to characterize the flux and power generated at vertical cracks in VT experiments, will be helpful to understand the interrelationship between strain and heat production in VT and may contribute for further development of the technique. Now, the next step is to analyze inclined samples, which is presented in chapter 4.

4 Characterization of slanted buried planar heat sources

4.1 Introduction

In this chapter, we present a first approximation to extend previous works [60, 66] (in time domain) with the aim of characterizing any type of planar defect of arbitrary inclination, using infrared thermography with a laser beam excitation that makes the defect behave as a heat source.

As a first step, we calculate the evolution of the surface temperature distribution produced by step-heated slanted buried planar heat sources of sample and we present simulations to illustrate the effect of the dimensions, depth and inclination on the surface temperature distribution. Finally, we prepare 3D printed plastic (optically transparent) parallelepiped samples, containing embedded graphite slabs of different inclinations. The results of the experiments have been compared with the predictions of the theory and a good agreement has been found.

4.2 Theory

We calculated the evolution of the surface temperature distribution produced by a rectangular heat source of width w and height h contained in plane that makes an angle ϕ with the sample surface. The upper side of the rectangle is buried at a depth d . The rectangle emits a constant and homogeneous heat flux of intensity I_o during a time interval τ and the sample is assumed as semi-infinite and under adiabatic conditions at the surface. The geometry is shown in Fig. 4.1

The temperature at the surface of a material of thermal conductivity, k , and diffusivity, α , can be easily obtained by generalizing the calculation corresponding to a vertical

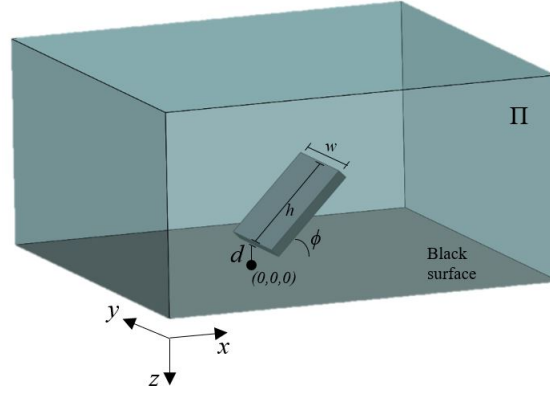


Figure 4.1: Geometry of a rectangular heat source of width w and height h contained in plane Π that makes an angle with the surface. The upper side of the rectangle is buried at a depth d below the surface

heat source [60]:

$$T_1(r_{z=0}, t) = \int_{-w/2}^{w/2} \int_0^{h \cos \phi} \frac{I_o}{2\pi k} \frac{\sqrt{1+m^2}}{\sqrt{(x-x')^2 + (y-y')^2 + (z-(mx'-d))^2}} \times \operatorname{Erfc} \frac{\sqrt{(x-x')^2 + (y-y')^2 + (z-(mx'-d))^2}}{\sqrt{4\alpha t}} dx' dy' \quad 0 \leq t \leq \tau \quad (4.1)$$

$$T_1(r_{z=0}, t) = \int_{-w/2}^{w/2} \int_0^{h \cos \phi} \frac{I_o}{2\pi k} \frac{\sqrt{1+m^2}}{\sqrt{(x-x')^2 + (y-y')^2 + (z-(mx'-d))^2}} \times \left[\operatorname{Erfc} \frac{\sqrt{(x-x')^2 + (y-y')^2 + (z-(mx'-d))^2}}{\sqrt{4\alpha t}} - \operatorname{Erfc} \frac{\sqrt{(x-x')^2 + (y-y')^2 + (z-(mx'-d))^2}}{\sqrt{4\alpha(t-\tau)}} \right] dx' dy' \quad t \geq \tau \quad (4.2)$$

where $m = \tan \phi$.

4.3 Simulations

Below we will show some simulations that we carry out in order to see the influence of the crack inclination parameter on the temperature for different inclinations and depths. All surface temperature data are normalized to the temperature value at the origin of coordinates and at the end of the burst $T_n = \frac{T(x,y,0,t)}{T(0,0,0,\tau)}$. The material parameters used in the simulations are those of photopolymer resin PR48 ($\alpha = 0.13\text{mm}^2/\text{s}$, $k = 0.24\text{W}/\text{mK}$), the material our samples are made of.

For the different inclinations: For inclinations of 0° , 20° , 45° and 70° , in the Fig. 4.2 we present the natural logarithms of the evolution of normalized temperature as a function of the time calculated at at $(0,0,0)$. The crack dimensions were: $w = 2\text{mm}$, $h = 2\text{mm}$ and buried at $d = 2\text{mm}$. The burst durations in Fig. 4.2 are a) $\tau=5\text{s}$ and b) $\tau=50\text{s}$. Both images (a y b) show that the inclination is very noticeable in the cooling parts of curve.

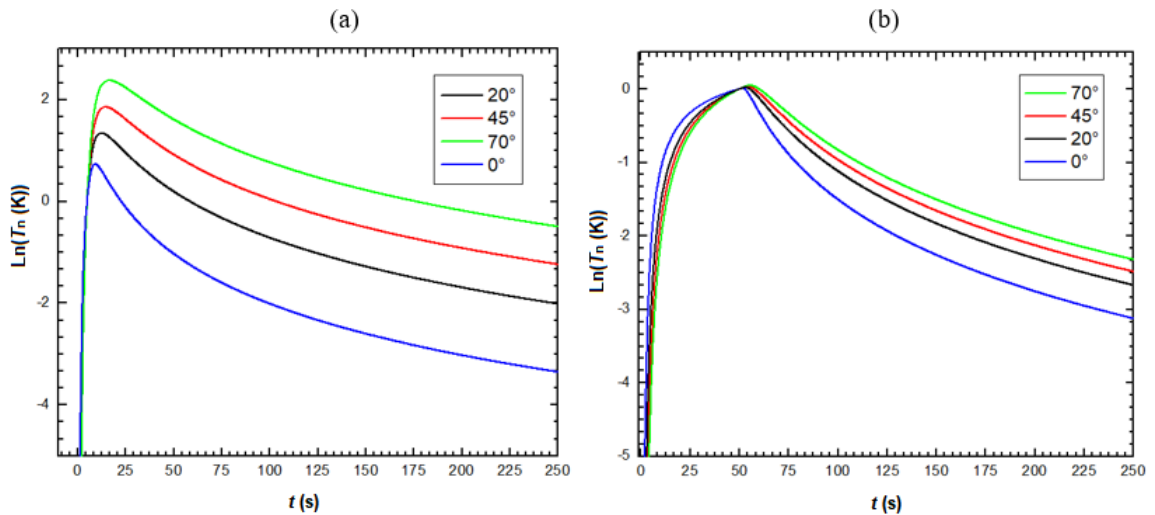


Figure 4.2: Natural logarithms of synthetic temperature to different inclinations for data corresponding to a breaking crack of width $w = 2\text{mm}$ and height $h = 2\text{mm}$ and buried at $d = 2\text{mm}$, for two burst durations: (a) $\tau = 5\text{s}$ and (b) $\tau = 50\text{s}$

The Fig. 4.3 shows natural logarithms of the normalized temperature, along the OX. It is noticeable the different inclinations: the inclination shows a effect important in the

maximum of the curve. In the image you can see an asymmetry with respect to the x axis for each inclination. When the sample is tilted, its maximum heat point runs in the direction of the x axis. Something that would not be visualized if it is plotted with respect to the y axis.

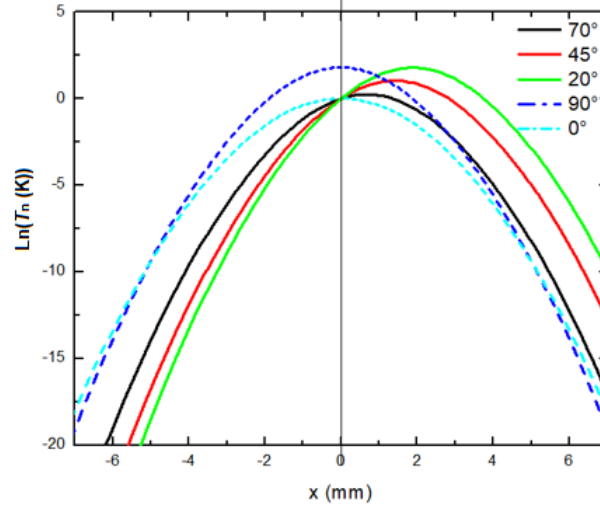


Figure 4.3: Simulation natural logarithms of the normalized temperature, along the OX for a breaking crack of width $w = 2\text{mm}$ and height $h = 2\text{mm}$ and buried at $d = 2\text{mm}$, calculated for burst durations of $\tau = 5\text{s}$.

For different depths: The Fig. 4.4 and Fig. 4.5 show the natural logarithms of the normalized temperature for different depths with 45° inclination along the x axis and as a function of time respectively. The crack dimensions is the same: $w = 2\text{mm}$, $h = 2\text{mm}$ and buried at 1mm, 2 mm, 5 mm and 10 mm.

For different burst durations the results seems to be very similar to those reported elsewhere [66]. Fig. 4.4 and Fig. 4.5 showing that the time graphs are more useful to discriminate between cracks located at different depths, i.e., it indicates that the effect of depth is very noticeable in the timing graphs, actually, for the deepest crack and the shorter burst duration, the maximum temperature rise occurs after the burst is over. The timing graph (Fig. 4.5b) during the cooling period is sensitive to the height of the heat source

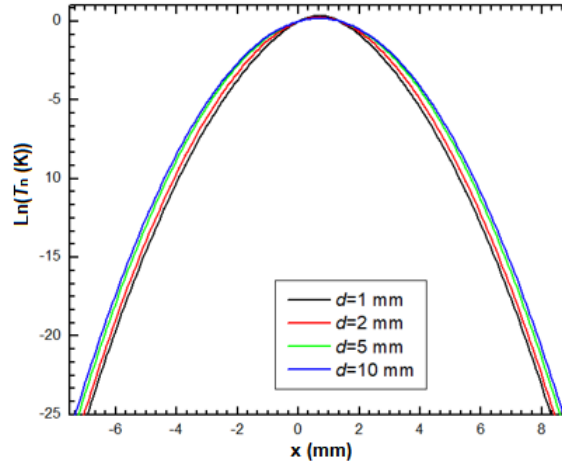


Figure 4.4: Natural logarithms of the normalized temperature calculated at $\tau = 5$ s along of X-axis for a crack with the same dimensions of the Fig. 4.2 but different distance to the surface (depths) and 45° inclination.

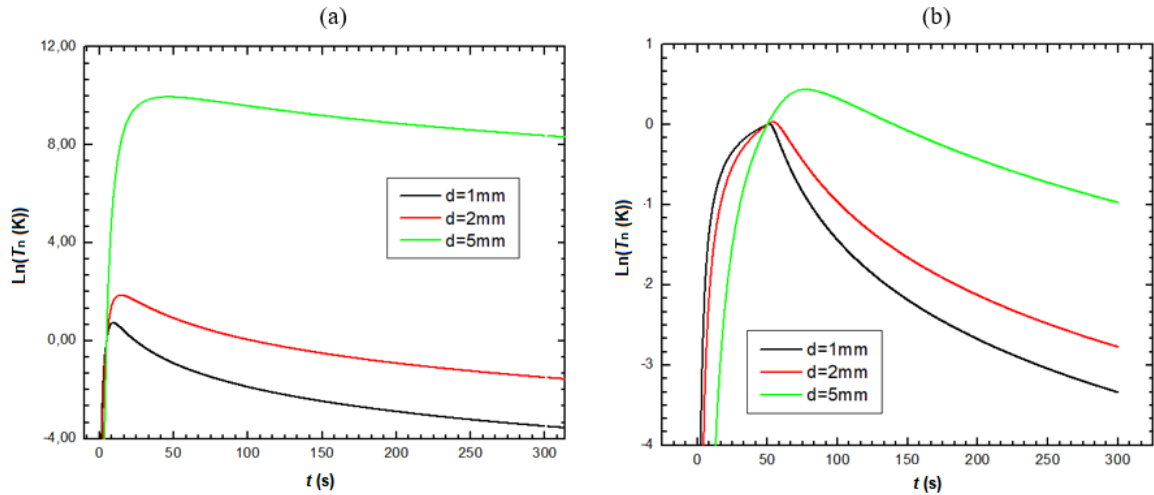


Figure 4.5: The evolution of the normalized temperature calculated at $(0,0,0)$ as a function of the time for a crack with the same dimensions of the Fig. 4.2 but different distance to the surface and 45° inclination. (a) $\tau = 5$ s and (b) $\tau = 50$ s

For different bursts: In the Fig. 4.6 these simulations suggest that any burst duration might be adequate to retrieve the dimensions of the inclinate rectangular crack.

However, we must take into account For long bursts, the timing graphs become less sensitive since the “effective distance” of all the locations in the heat sources is small compared to the thermal diffusion length associated to the burst duration $L_c = \sqrt{\tau\alpha}$ [22].

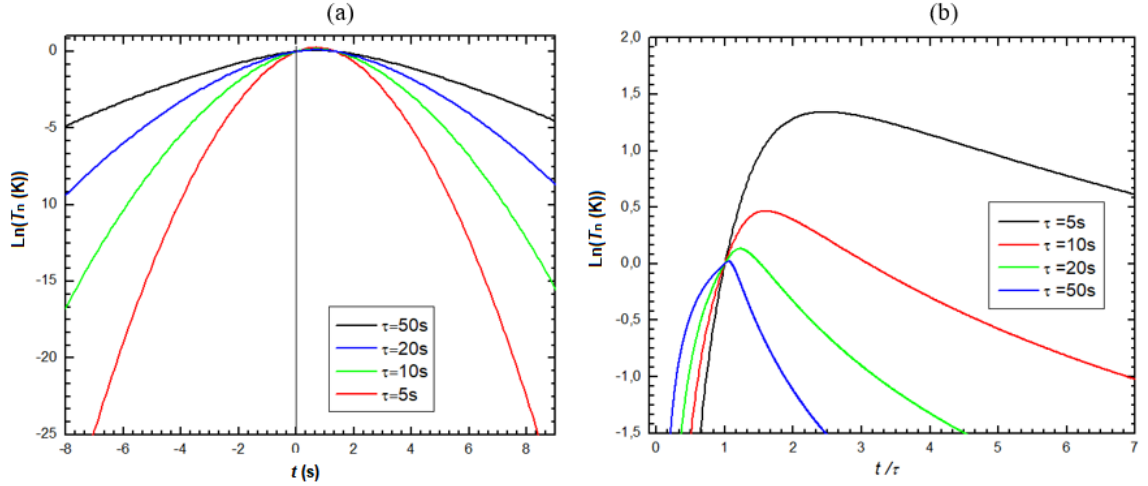


Figure 4.6: (a) Natural logarithms of the normalized temperature calculated at $t = \tau$, a profile along of X-axis, for a a breaking crack of width $w = 2\text{mm}$ and height $h = 2\text{mm}$ with inclination (20°) but for different burst. And (b) the evolution of the normalized temperature calculated at $(0,0,0)$ as a function of the normalized time, t/τ .

4.4 Experiments

In order to check the ability of the method to characterize inclined cracks, we have prepared 3D printed photopolymer resin (PR48) rectangular blocks (shown as Π in the Fig. 4.7) containing embedded $100\ \mu\text{m}$ thick graphite slabs of square shape ($L = 1,8\text{mm}$) and different inclinations with respect to the surface. The shortest distance of the slabs to the blackened surface of the block is d . This front surface was painted black to increase optical emissivity for thermographic purposes. The PR48 is optically transparent in the visible spectral region, allowing the excitation of the graphite slabs from the sample’s rear or lateral side depending on the inclination, using a diode laser emitting at 530nm and power $P = 200\text{mW}$. Care was taken in order to assure uniform illumination of the slab and to avoid undesirable light absorption by the black surface.

4.4 Experiments

The time duration of the excitation was 20s and 40s . The thermal diffusivity, α , and the effusivity, ε , of the PR48 material were determined by the photopyroelectric (PPE) technique in the back [74] and front [75] detection configuration, respectively. The obtained values were $\alpha = 0.13\text{mm}^2/\text{s}$ and $\varepsilon = 660\text{Js}^{-1/2}\text{K}^{-1}\text{m}^{-2}$, from which the thermal conductivity was calculated as $k = \varepsilon\sqrt{\alpha} = 0.24\text{W/mK}$.

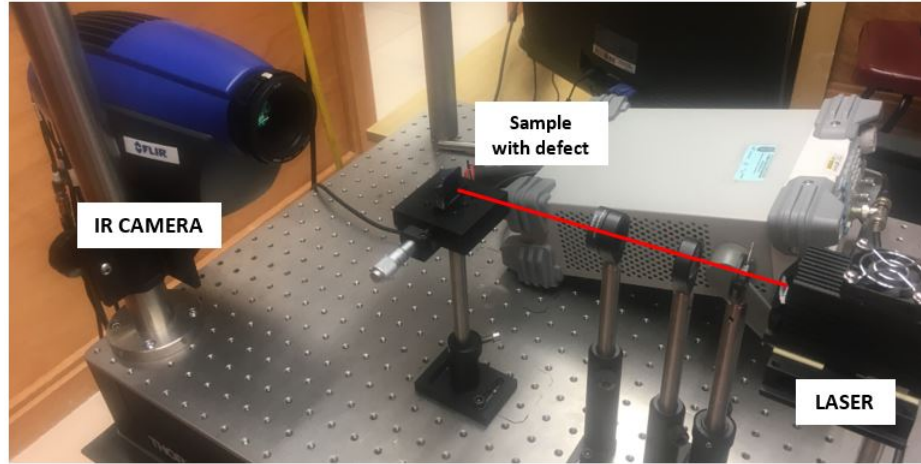


Figure 4.7: Photograph of the experimental set-up

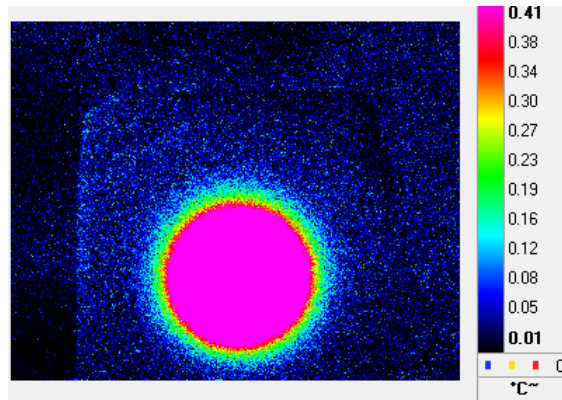


Figure 4.8: Thermal image of sample (20°) at $t = \tau = 20\text{s}$

Thermographs from the blackened surface were collected from the very beginning of the excitation, using a FLIR SC 5000 camera with framerate of 25Hz and each pixel in

the detector averages the temperature over a $90\ \mu\text{m}$ side square in the sample surface. The Fig. 4.8 shows a thermal image typical of the samples.

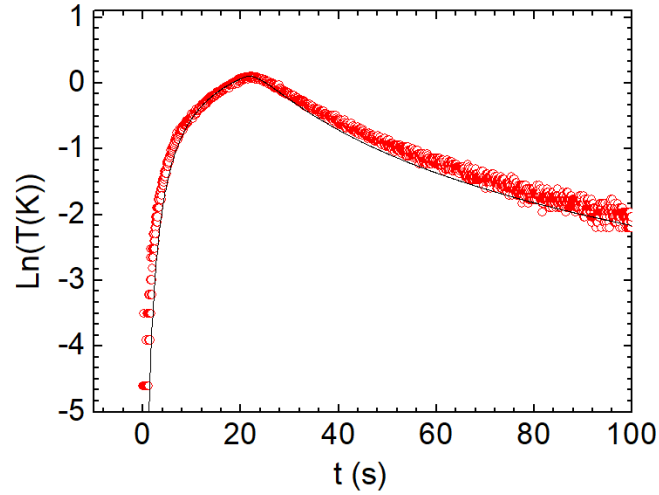


Figure 4.9: Evolution of the normalized temperature calculated at $(0,0,0)$ as a function of the time for 20° and burst $\tau=20\text{s}$.

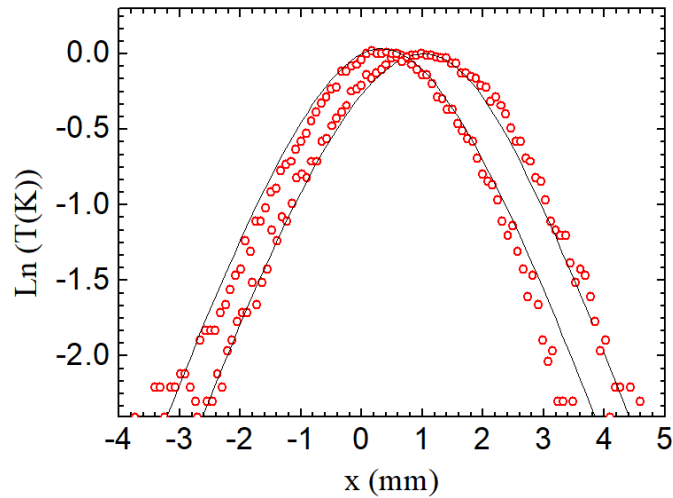


Figure 4.10: Natural logarithms of the normalized temperature calculated at $t = \tau=20\text{s}$, a profile along of X-axis and different inclination (left 70° , right 20°)

Next, some experiments will be shown which validate the information of the simulations. The fitting program is still being worked on, so that only experimental data are

presented together with the theoretical values. Despite not being fittings the results are quite good. We analyzed both temperature versus time (Fig. 4.9), and along the X and Y axes (Fig. 4.10, Fig. 4.11). The crack dimensions were: $w = 2\text{mm}$, $h = 2\text{mm}$. The sample of 70° inclination is buried at $d = 1.8\text{mm}$ and of 20° inclination is buried at $d = 2\text{mm}$.

In the Fig. 4.11 we can see the influence of the inclination in the results. In effect, regardless of the burst the difference between the inclinations is still appreciating.

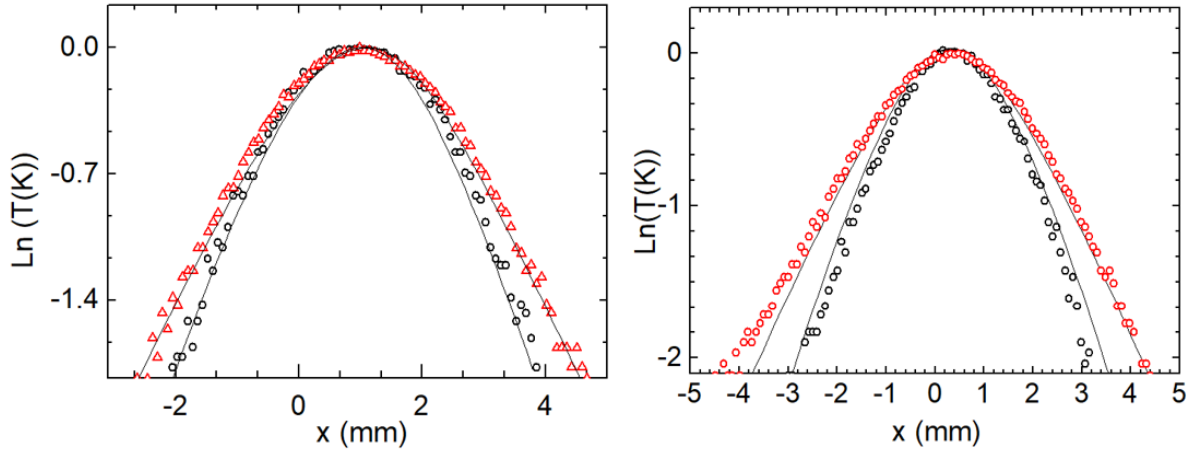


Figure 4.11: Natural logarithms of the normalized temperature calculated at $t = \tau$, a profile along of X-axis, with inclination 20° (left) and 70° (right) for different burst (black circle: 20s and red: 40s)

4.5 Conclusions

The surface temperature simulations obtained for different inclinations and depths of the crack indicate that, the inclination of the crack could be determined in the future. It has been shown that the surface temperature is sensitive to the inclination and depth of the heat source, the experimental data are in good agreement with the predictions of the model and this allows us to think that in the future it will be possible to characterize the heat sources from the information you have shown (Timing graph and thermogram). For this the development of different algorithms is mandatory. Work in this direction is underway.

Conclusions

It was designed and implemented an experimental set-up for active thermography measurements in front and rear detection configurations. With this experimental system, thermally thick samples were characterized (thermal diffusivity) and the influence of heat losses by convection and radiation on bad conductors was observed not only in amplitude as in previous works but also in the signal phase. It was shown that CRHL become significant at low modulation frequencies for low thermal conductivity materials. It is observed that there is influence of CRHL in the signal phase too. The here presented results should be helpful not only for researchers in the field of photothermal techniques, but also for those dealing with any phenomena involving periodical modulated heating of samples.

On the other hand, it has been demonstrated that the results indicate that it is possible to characterize both the heat flux distribution and the thermal power emitted by cracks in VT experiments. It was shown by computer simulations aided with experiments involving excitation with light that it is possible to characterize oblique cracks. Also, the angle of inclination can be detected in the graphs of timing graph and especially in the distribution of temperature along the x and y axis.

The work carried out throughout this thesis serves as the basis for future lines of research related to thermal characterization of materials and imaging and reconstruction of cracks of any shape and in any position. The experimental system of chapter 2 allows to work in vacuum, opening the way to be able to characterize in a future thin films, filaments, anisotropic materials, among others. Regarding chapters 3 and 4, with these contributions it is observed that the characterization of real cracks is getting closer. Now, the most immediate interest is in using the inversion algorithm for the characterization of inclined cracks instead of vertical ones and for the reduction of shadowing present in the reconstruction of certain geometries.

Products

Articles:

A. Mendioroz, **K. Martínez**, R. Celorrio, A. Salazar. Characterizing the shape and heat production of open vertical cracks in burst vibrothermography experiments. *NDT & E International* (2018).

N. Camacho, J.F. May-Crespo, J.B. Rojas-Trigos, **K. Martínez**, J. Barcena, A.A. Segundo, Evaluation of Thermal Properties of Epoxy-Alumina and Epoxy-Zinc Oxide Composites. *J. of Materials Sci. & Technology*. (Sent)

E. Serrano, H. Martinez, **K. J. Martínez**, E. Marín, F. Juárez, Densification and microstructure of spark plasma sintered 7YSZ–Gd₂O₃ ceramic nano-composites, *J. of Asian Ceramic Soc.* 5, 266. (2017)

K. Martínez, E. Marín, C. Glorieux, A. Lara-Bernal, A. Calderón, G. P. Rodríguez, and R. Ivanov, Thermal diffusivity measurements in solids by photothermal infrared radiometry: Influence of convection–radiation heat losses, *Int. J. Therm. Sci.* 98, 202. (2015)

Proceedings:

K. Martínez, R. Celorrio, A. Mendioroz. Characterization of open cracks in burst vibrothermography experiments. Proceedings of the 14th Quantitative InfraRed Thermography Conference, QIRT 2018, Berlin, Germany, 25-29 June 2018, pp 463-471 DOI: 10.21611/qirt.2018.042

J. Jaime, A. Cifuentes, K. Martínez, E. Marin, J. Hernandez-Wong, A. Mendioroz, A. Salazar Application of the Hill Climbing Algorithm to the Geometrical Reconstruction of Vertical Buried Heat Sources Using Vibrothermography Proceedings of the 14th Quantitative InfraRed Thermography Conference, QIRT 2018, Berlin, Germany, 25-29 June 2018, pp 168-171 DOI: 10.21611/qirt.2018.p41

A. Mendioroz, A. Salazar, K. Martinez, A. Cifuentes, E. Marín, R. Celorrio, P. Venegas, I. Sáez de Ocáriz Characterization of slanted buried planar heat sources using time domain Infrared Thermography Proceedings of the 14th Quantitative InfraRed Thermography Conference, QIRT 2018, Berlin, Germany, 25-29 June 2018, pp 563-564 DOI: 10.21611/qirt.2018.059

Awards:

E. Grinzato Award, 14th Quantitative InfraRed Thermography. Berlin, Germany. Best presentation and paper.

Research Stay:

Pulse active infrared thermography, Universidad del País Vasco, Laboratorio de Técnicas Fototérmicas, Bilbao, Spain.

Conferences Presentations:

Characterization of open and kissing vertical cracks using vibrothermography. 10th International Symposium on NDT in Aerospace, (Oct 24-26, 2018) Dresde, Germany.

Characterization of thin samples with rear and frontal configuration using lock-in thermography. XI International Conference on Surfaces, Materials and Vacuum, (Sept 24-28, 2018) Playa del Carmen, Mexico.

Characterization of open cracks in burst vibrothermography experiments. 14th Quantitative InfraRed Thermography Conference, (Jun 25-29, 2018) Berlin, Germany.

Characterizing non-compact vertical heat sources with burst vibrothermography technique. 19th International Conference on Photoacoustic and Photothermal Phenomena. (Jul 16-20, 2017) Bilbao, Spain.

Influence of heat losses at low frequencies in photothermal experiments. XXVI International Materials Research Congress, (Aug 20-25, 2017) Cancún, Mexico.

Measurement of thermal diffusivity by lock-in thermography: Analysis of heat loss by convection and radiation on the phase. 4th Mediterranean International Workshop on Photoacoustic & Photothermal Phenomena. (Oct 19-26, 2016) Erice, Italy.

A method for measurement thermal diffusivity of low thermal conductivity solids using infrared detection. XXIV International Materials Research Congress, (Aug 216-20, 2015) Cancún, Mexico.

Bibliography

- [1] W. Herschel, “Xv. experiments on the solar, and on the terrestrial rays that occasion heat; with a comparative view of the laws to which light and heat, or rather the rays which occasion them, are subject, in order to determine whether they are the same, or different,” *Philosophical Transactions of the royal Society of London*, vol. 90, pp. 293–326, 1800.
- [2] M. Vollmer and K.-P. Möllmann, *Infrared thermal imaging: fundamentals, research and applications*. John Wiley & Sons, 2017.
- [3] C. Ibarra-Castanedo, J. R. Tarpani, and X. P. Maldague, “Nondestructive testing with thermography,” *European Journal of Physics*, vol. 34, no. 6, p. S91, 2013.
- [4] P. Laloue, C. Bissieux, J.-F. Henry, H. Pron, J. L’Ecolier, and F. Nigon, “Infrared nondestructive measurement of thermal resistance between liner and engine block: design of experiment,” *International Journal of Thermal Sciences*, vol. 47, no. 3, pp. 249–260, 2008.
- [5] S. Bagavathiappan, B. Lahiri, T. Saravanan, J. Philip, and T. Jayakumar, “Infrared thermography for condition monitoring—a review,” *Infrared Physics & Technology*, vol. 60, pp. 35–55, 2013.
- [6] A. N. Huda and S. Taib, “Application of infrared thermography for predictive/preventive maintenance of thermal defect in electrical equipment,” *Applied Thermal Engineering*, vol. 61, no. 2, pp. 220–227, 2013.
- [7] M. C. Eti, S. Ogaji, and S. Probert, “Reducing the cost of preventive maintenance (pm) through adopting a proactive reliability-focused culture,” *Applied energy*, vol. 83, no. 11, pp. 1235–1248, 2006.
- [8] A. Al-Habaibeh, F. Zorriassatine, and N. Gindy, “Comprehensive experimental evaluation of a systematic approach for cost effective and rapid design of condition monitoring systems using taguchi’s method,” *Journal of Materials Processing Technology*, vol. 124, no. 3, pp. 372–383, 2002.
- [9] E. Johnson, P. Hyer, P. Culotta, and I. Clark, “Evaluation of infrared thermography as a diagnostic tool in cvd applications,” *Journal of crystal growth*, vol. 187, no. 3-4, pp. 463–473, 1998.
- [10] F. Mercuri, U. Zammit, N. Orazi, S. Paoloni, M. Marinelli, and F. Scudieri, “Active infrared thermography applied to the investigation of art and historic artefacts,” *Journal of thermal analysis and calorimetry*, vol. 104, no. 2, p. 475, 2011.

- [11] R. L. Thomas, L. D. Favro, X. Han, Z. Ouyang, H. Sui, and G. Sun, "Infrared imaging of ultrasonically excited subsurface defects in materials," May 22 2001, uS Patent 6,236,049.
- [12] L. Favro, T. Ahmed, X. Han, L. Wang, X. Wang, Y. Wang, P. Kuo, R. Thomas, and S. Shephard, "Thermal wave imaging of aircraft structures," in *Review of Progress in Quantitative NonDestructive Evaluation*. Springer, 1995, pp. 461–466.
- [13] X. Maldague, "Theory and practice of infrared technology for nondestructive testing," 2001.
- [14] G. C. Holst, *Common sense approach to thermal imaging*. SPIE Optical Engineering Press Washington, 2000.
- [15] C. Meola, *Infrared thermography recent advances and future trends*. Bentham Science Publishers, 2012.
- [16] C. Ibarra-Castanedo and X. P. Maldague, "Infrared thermography," in *Handbook of technical diagnostics*. Springer, 2013, pp. 175–220.
- [17] A. Castelo Varela, "Characterization of vertical cracks using lock-in vibrothermography," Ph.D. dissertation, Universidad del País Vasco, 2017.
- [18] G. Tessier, *Photothermal Techniques*. Berlin, Heidelberg: Springer Berlin Heidelberg, 2009, pp. 389–409. [Online]. Available: http://dx.doi.org/10.1007/978-3-642-04258-4_13
- [19] E. Marín, "Basic principles of thermal wave physics and related techniques," 2013.
- [20] A. Salazar, "Aplicación de las técnicas fototérmicas al estudio de materiales," *Boletín de la Sociedad Española de Cerámica y Vidrio*, vol. 39, no. 4, pp. 584–588, 2000.
- [21] A. Mandelis, "Laser infrared photothermal radiometry of semiconductors: principles and applications to solid state electronics," *Solid State Electronics*, vol. 42, no. 1, pp. 1–15, 1998.
- [22] D. P. Almond and P. Patel, *Photothermal science and techniques*. Springer Science & Business Media, 1996, vol. 10.
- [23] G. Rousset, F. Charbonnier, and F. Lepoutre, "Influence of radiative and convective transfers in a photothermal experiment," *Journal of applied physics*, vol. 56, no. 7, pp. 2093–2096, 1984.
- [24] R. D. Cowan, "Proposed method of measuring thermal diffusivity at high temperatures," *Journal of Applied Physics*, vol. 32, no. 7, pp. 1363–1370, 1961.
- [25] B. Zhang and R. Imhof, "Theoretical analysis of the surface thermal wave technique for measuring the thermal diffusivity of thin slabs," *Applied Physics A*, vol. 62, no. 4, pp. 323–334, 1996.

- [26] E. Marín, A. Lara-Bernal, A. Calderón, and O. Delgado-Vasallo, “On the heat transfer through a solid slab heated uniformly and continuously on one of its surfaces,” *European Journal of Physics*, vol. 32, no. 3, p. 783, 2011.
- [27] O. Delgado-Vasallo and E. Marín, “On the criterion for neglecting convective effects in photoacoustic experiments,” in *Journal de Physique IV (Proceedings)*, vol. 125. EDP sciences, 2005, pp. 165–167.
- [28] I. Solodov, J. Bai, S. Bekgulyan, and G. Busse, “A local defect resonance to enhance acoustic wave-defect interaction in ultrasonic nondestructive evaluation,” *Applied Physics Letters*, vol. 99, no. 21, p. 211911, 2011.
- [29] J. N. Zalameda, W. P. Winfree, and W. T. Yost, “Air coupled acoustic thermography (acat) inspection technique,” in *AIP Conference Proceedings*, vol. 975, no. 1. AIP, 2008, pp. 467–474.
- [30] S. Sathish, J. T. Welter, K. V. Jata, N. Schehl, and T. Boehnlein, “Development of nondestructive non-contact acousto-thermal evaluation technique for damage detection in materials,” *Review of Scientific Instruments*, vol. 83, no. 9, p. 095103, 2012.
- [31] T. L. Bergman, F. P. Incropera, D. P. DeWitt, and A. S. Lavine, *Fundamentals of heat and mass transfer*. John Wiley & Sons, 2011.
- [32] Y. A. Āngengel, *Thermodynamics and heat transfer*. McGraw-Hill, 2008, vol. 2.
- [33] P. Chen, “Applications of photothermal radiometry at low frequencies,” 1994.
- [34] E. Marín, “Linear relationships in heat transfer,” *Latin-American Journal of Physics Education*, vol. 3, no. 2, p. 9, 2009.
- [35] A. Rosenwaig, J. Opsal, W. L. Smith, and D. Willenborg, “Detection of thermal waves through optical reflectance,” *Applied Physics Letters*, vol. 46, no. 11, pp. 1013–1015, 1985.
- [36] A. Salazar, “Energy propagation of thermal waves,” *European journal of physics*, vol. 27, no. 6, p. 1349, 2006.
- [37] B. Bein and J. Pelzl, “Analysis of surfaces exposed to plasmas by nondestructive photoacoustic and photothermal techniques,” in *Plasma Diagnostics: Surface Analysis and Interactions*. Elsevier, 1989, pp. 211–326.
- [38] A. Salazar, A. Mendioroz, and R. Fuente, “The strong influence of heat losses on the accurate measurement of thermal diffusivity using lock-in thermography,” *Applied Physics Letters*, vol. 95, no. 12, p. 121905, 2009.
- [39] A. Ångstrom, “Neue methode, das wärmeleitungsvermögen der körper zu bestimmen,” *Annalen der Physik*, vol. 190, no. 12, pp. 513–530, 1862.
- [40] E. Marín, L. Jean-Baptiste, and M. Hernández, “Teaching thermal wave physics with soils,” *Revista mexicana de física E*, vol. 52, no. 1, pp. 21–27, 2006.

- [41] A. Salazar and A. Mendioroz, "Propagation of thermal waves across a wedge," *Journal of Applied Physics*, vol. 112, no. 6, p. 063511, 2012.
- [42] H. Carslaw and J. Jaeger, *Conduction of heat in solids: Oxford Science Publications*. Oxford, England, 1959.
- [43] S. Volz, *Microscale and nanoscale heat transfer*. Springer, 2007.
- [44] C. Ibarra-Castanedo, M. Genest, J.-M. Piau, S. Guibert, A. Bendada, and X. P. Maldague, "Active infrared thermography techniques for the nondestructive testing of materials," in *Ultrasonic and advanced methods for nondestructive testing and material characterization*. World Scientific, 2007, pp. 325–348.
- [45] P. Capper and C. Elliott, *Infrared detectors and emitters: materials and devices*. Springer Science & Business Media, 2013, vol. 8.
- [46] E. Marin and R. Ivanov, "Lia in a nut shell: How can trigonometry help to understand lock-in amplifier operation?" *Latin-American Journal of Physics Education*, vol. 3, no. 3, p. 7, 2009.
- [47] O. Breitenstein, W. Warta, and M. Langenkamp, *Lock-in thermography: Basics and use for evaluating electronic devices and materials*. Springer Science & Business Media, 2010, vol. 10.
- [48] S. W. Smith, "Digital signal processing, a practical guide for scientists and engineers," *New York: Newnes*, 2003.
- [49] A. Cifuentes Castro, "Contribución a la caracterización térmica de materiales y detección de defectos sub-superficiales utilizando termografía infrarroja y otros métodos de generación de imágenes," Ph.D. dissertation, Instituto Politécnico Nacional, 2017.
- [50] D. Wu, T. Zweschper, A. Salerno, and G. Busse, "Lock-in thermography for non-destructive evaluation of aerospace structures," *NDT. net*, vol. 3, no. 9, 1998.
- [51] E. G. Henneke, K. L. Reifsnider, and W. W. Stinchcomb, "Thermography—Tandem method for damage detection," *JOM*, vol. 31, no. 9, pp. 11–15, 1979.
- [52] E. Henneke and T. Jones, "Detection of damage in composite materials by vibrothermography," 1979.
- [53] K. Reifsnider, E. G. Henneke, and W. Stinchcomb, "The mechanics of vibrothermography," in *Mechanics of nondestructive testing*. Springer, 1980, pp. 249–276.
- [54] J. Renshaw, J. C. Chen, S. D. Holland, and R. B. Thompson, "The sources of heat generation in vibrothermography," *NDT & E International*, vol. 44, no. 8, pp. 736–739, 2011.
- [55] X. Maldague and S. Marinetti, "Pulse phase infrared thermography," *Journal of applied physics*, vol. 79, no. 5, pp. 2694–2698, 1996.

- [56] K. Martínez, E. Marín, C. Glorieux, A. Lara-Bernal, A. Calderón, G. P. Rodríguez, and R. Ivanov, “Thermal diffusivity measurements in solids by photothermal infrared radiometry: Influence of convection–radiation heat losses,” *International Journal of Thermal Sciences*, vol. 98, pp. 202–207, 2015.
- [57] A. Salazar, E. Apiñaniz, A. Mendioroz, and A. Oleaga, “A thermal paradox: which gets warmer?” *European Journal of Physics*, vol. 31, no. 5, p. 1053, 2010.
- [58] E. Serrano Pérez, H. Martínez Gutierrez, K. Martínez Gonzalez, E. Marin Moares, and F. Juarez Lopez, “Densification and microstructure of spark plasma sintered 7ysz–gd2o3 ceramic nano-composites,” *Journal of Asian Ceramic Societies*, vol. 5, no. 3, pp. 266–275, 2017.
- [59] N. Camacho, J. May-Crespo, J. Rojas-Trigos, K. Martínez, J. Barcena, A. Segundo, and E. Marin, “Evaluation of thermal properties of epoxy-alumina and epoxy-zinc oxide composites,” *Journal of Materials Science and Technology*.
- [60] A. Mendioroz, R. Celorrio, A. Cifuentes, L. Zatón, and A. Salazar, “Sizing vertical cracks using burst vibrothermography,” *NDT & E International*, vol. 84, pp. 36–46, 2016.
- [61] A. Castelo, A. Mendioroz, R. Celorrio, and A. Salazar, “Optimizing the inversion protocol to determine the geometry of vertical cracks from lock-in vibrothermography,” *Journal of Nondestructive Evaluation*, vol. 36, no. 1, p. 3, 2017.
- [62] A. Mendioroz, E. Apiñaniz, A. Salazar, P. Venegas, and I. Sáez-Ocáriz, “Quantitative study of buried heat sources by lock-in vibrothermography: an approach to crack characterization,” *Journal of Physics D: Applied Physics*, vol. 42, no. 5, p. 055502, 2009.
- [63] A. Mendioroz, A. Castelo, R. Celorrio, and A. Salazar, “Characterization of vertical buried defects using lock-in vibrothermography: I. direct problem,” *Measurement Science and Technology*, vol. 24, no. 6, p. 065601, 2013.
- [64] —, “Characterization and spatial resolution of cracks using lock-in vibrothermography,” *NDT & E International*, vol. 66, pp. 8–15, 2014.
- [65] R. Celorrio, A. Mendioroz, and A. Salazar, “Characterization of vertical buried defects using lock-in vibrothermography: II. inverse problem,” *Measurement Science and Technology*, vol. 24, no. 6, p. 065602, 2013.
- [66] A. Mendioroz, R. Celorrio, and A. Salazar, “Characterization of rectangular vertical cracks using burst vibrothermography,” *Review of Scientific Instruments*, vol. 86, no. 6, p. 064903, 2015.
- [67] J. Renshaw, S. D. Holland, and R. B. Thompson, “Measurement of crack opening stresses and crack closure stress profiles from heat generation in vibrating cracks,” *Applied Physics Letters*, vol. 93, no. 8, p. 081914, 2008.

- [68] S. D. Holland, “Thermographic signal reconstruction for vibrothermography,” *Infrared Physics & Technology*, vol. 54, no. 6, pp. 503–511, 2011.
- [69] H. W. Engl, M. Hanke, and A. Neubauer, *Regularization of inverse problems*. Springer Science & Business Media, 1996, vol. 375.
- [70] C. Brune, A. Sawatzky, and M. Burger, “Primal and dual bregman methods with application to optical nanoscopy,” *International Journal of Computer Vision*, vol. 92, no. 2, pp. 211–229, 2011.
- [71] I. Daubechies, M. Defrise, and C. De Mol, “An iterative thresholding algorithm for linear inverse problems with a sparsity constraint,” *Communications on Pure and Applied Mathematics: A Journal Issued by the Courant Institute of Mathematical Sciences*, vol. 57, no. 11, pp. 1413–1457, 2004.
- [72] S. W. Anzengruber and R. Ramlau, “Morozov’s discrepancy principle for tikhonov-type functionals with nonlinear operators,” *Inverse Problems*, vol. 26, no. 2, p. 025001, 2009.
- [73] K. Martínez, R. Celorrio, and A. Mendioroz, “Characterization of open cracks in burst vibrothermography experiments.” *Quantitative InfraRed Thermography Journal*, vol. 0, no. 0, pp. 463–471, 2018.
- [74] U. Zammit, F. Mercuri, S. Paoloni, and R. Pizzoferrato, “Thermophysical parameters evaluation by pyroelectric detection,” *International Journal of Thermophysics*, vol. 39, no. 11, p. 122, 2018.
- [75] D. Dadarlat and C. Neamtu, “High performance photopyroelectric calorimetry of liquids.” *Acta Chimica Slovenica*, vol. 56, no. 1, 2009.